

METEOTSUNAMI OCCURRENCE AND PROPAGATION IN THE NORTHEASTERN
GULF OF MEXICO

By

MATLACK E. GILLIN

A THESIS PRESENTED TO THE GRADUATE SCHOOL
OF THE UNIVERSITY OF FLORIDA IN PARTIAL FULFILLMENT
OF THE REQUIREMENTS FOR THE DEGREE OF
MASTER OF ENGINEERING

UNIVERSITY OF FLORIDA

2017

© 2017 Matlack E. Gillin

To my wife, Bethany, for her steadfast support and encouragement

ACKNOWLEDGMENTS

I would like to acknowledge the support I have received from my advisor, Dr. Arnaldo Valle-Levinson, and my committee member, Dr. Maitane Olabarrieta. I also acknowledge Dr. Charles and Lucinda Carlson for accepting me as their own son and loving me despite my shortcomings. And lastly, I would like to thank my parents, Jeanne M. Huffman and James J. Gillin for providing me every opportunity to succeed in my upbringing.

TABLE OF CONTENTS

	<u>page</u>
ACKNOWLEDGMENTS.....	4
LIST OF FIGURES.....	6
ABSTRACT	7
CHAPTER	
1 INTRODUCTION	9
2 METHODS.....	13
3 RESULTS	17
January 15, 2016	17
January 17, 2016	22
4 DISCUSSION	51
5 CONCLUSION.....	56
LIST OF REFERENCES	57
BIOGRAPHICAL SKETCH.....	60

LIST OF FIGURES

<u>Figure</u>	<u>page</u>
2-1 Locations providing data for this study.	16
3-1 De-tided, filtered signal at 7 stations.....	27
3-2 Atmospheric conditions on January 15 th , 2016.....	28
3-3 Meteotsunami signal on January 15, 2016.....	29
3-4 January 15, 2016 wavelet analysis.....	30
3-5 Sketch of convection cells in the area behind a cold front together with a theoretical surface elevation response.	35
3-6 Filtered East-West wind record at PCB on January 15 th , 2017.....	36
3-7 Wavelet analysis of wind signal on January 15, 2016 from PCB.....	37
3-8 Wavelet coherence analysis of wind signal on January 15, 2016 from PCB. Arrows indicate the phase difference between the two signals.....	38
3-9 Spatial representation of the Froude number for the meso-scale convective system on January 15, 2016.....	39
3-10 Atmospheric conditions on January 17 th , 2016.....	40
3-11 Meteotsunami signal on January 17, 2016.	41
3-12 January 17, 2016 wavelet analysis.....	42
3-13 Filtered East-West wind record at PCB on January 17 th , 2017.....	47
3-14 Wavelet analysis of wind signal on January 17, 2016 from PCB.	48
3-15 Wavelet coherence analysis of wind signal on January 17, 2016 from PCB. Arrows indicate the phase difference between the two signals.....	49
3-16 Spatial representation of the Froude number for the atmospheric system on January 17, 2016.....	50

Abstract of Thesis Presented to the Graduate School
of the University of Florida in Partial Fulfillment of the
Requirements for the Degree of Master of Engineering

METEOTSUNAMI OCCURRENCE AND PROPAGATION IN THE NORTHEASTERN
GULF OF MEXICO

By

Matlack E. Gillin

December 2017

Chair: Arnaldo Valle-Levinson

Major: Coastal and Oceanographic Engineering

Meteotsunamis occur globally but have only recently gained attention in the Gulf of Mexico. Records from NOAA sensors and additional instruments were used to examine water levels and atmospheric pressure forcing in the northeastern Gulf of Mexico from December 2015 to February 2016. This analysis identified two meteotsunami events, both of which were produced by an oscillatory pressure signal. Continuous Wavelet Transform analysis of water level and atmospheric pressure showed a remarkably similar structure in the frequency domain during both meteotsunamis. This qualitatively suggested a dependence of water level on atmospheric pressure. Additional wavelet coherence analysis showed that coherency existed between wind oscillations associated with convective cells and the meteotsunami water level. This indicated that both atmospheric pressure and wind played a role in meteotsunami generation. Vector addition using atmospheric pressure peaks and troughs yielded the speed and direction of these atmospheric disturbances. The velocity of these disturbances was used, along with the shallow water wave approximation, to identify the location of atmosphere-ocean resonance and the approximate position where these meteotsunamis became free waves. This technique

can be complemented with numerical modeling to quantify the wave conditions required to reproduce the coastline signals. This will allow future research to determine the required meteotsunami amplification in the resonance region.

CHAPTER 1 INTRODUCTION

Since its inception, the word 'tsunami,' translated in Japanese to 'harbor wave,' has been used interchangeably with 'seismically induced wave.' As tsunami research developed, this understanding was forced to shift due to the acknowledgment of submarine landslides, volcanic eruptions, and even meteorite impacts as generation mechanisms for common tsunamis. Beginning in 1996, however, the study of meteorological tsunamis, or meteotsunamis, has become prevalent within the tsunami community [Rabinovich and Monserrat, 1996]. *Natural Hazards* dedicated its entire October, 2014 issue to this phenomenon. Meteotsunamis develop from an atmospheric pressure disturbance that causes a perturbation in water level. This water level perturbation amplifies due to resonance effects [Monserrat et al., 2006]. Meteotsunamis have likely existed for centuries and have been assigned regional names such as rissaga in the Balearic Islands (literal translation: 'drying'), abiki in Japan ('net-dragging waves'), and marrubio in Sicily ('mad sea') [Candela et al., 1999; Vilibić et al., 2008; Asano et al., 2012]. In 1978, Vela Luka, Croatia was hit with an estimated 6m high wave that devastated the local town, causing the equivalent of \$27 million worth of damage [Monserrat et al, 2006]. In 2006, Ciutadella Harbor in Menorca, Spain, was inundated with a wave of approximately 4 m, destroying more than 40 boats and causing an estimate \$30 million euros of damage [Monserrat et al, 2006]. And in the U.S., a strong southward-propagating storm system passed over Daytona Beach, FL in 1992, generating a meteotsunami of

approximately 3 m. This event caused injuries to 75 people and damaged 12 vehicles [Churchill et al., 1995; Sallenger et al., 1995].

A meteotsunami has the same spatial and propagation characteristics of a seismically generated tsunami but differs in generation mechanism. These long waves (wavelengths > 20 times water depth) have periods of a few minutes to a few hours (typically not more than 3 hours) [Monserrat et al., 2006]. An important characteristic of meteotsunamis is that, due to their extensive wavelength, they behave as shallow water waves in coastal regions. As such, the speed of these waves is a function of the water depth. The depth-dependent phase speed of meteotsunamis means that resonance will occur in an area where depth remains largely constant.

In 2006, Monserrat et al. posited four meteotsunami generation requirements. The first of these requirements is the presence of a 2-6 hPa pressure change. This pressure change could be caused by an isolated pressure jump [Hibiya and Kajiura, 1982; Vilibic' et al., 2004, 2005] or by a train of atmospheric gravity waves [Gossard and Munk, 1954; Monserrat et al., 1991a; Garcies et al., 1996]. The second requirement is that the atmospheric disturbance must propagate in resonance with the shallow-water wave celerity. This resonance is most often associated with Proudman resonance, where the atmospheric disturbance translational speed equals the celerity of long ocean waves [Proudman, 1929]. Other means of resonance include Greenspan resonance and shelf resonance. In Greenspan resonance, the alongshore component of the atmospheric disturbance velocity equals the celerity of the j^{th}

mode of edge waves [Greenspan, 1956]. In shelf resonance, the atmospheric disturbance and associated ocean wave have periods and/or wavelengths equal to the resonant period and/or wavelength of the shelf region [Monserrat et al, 2006]. These resonance effects are best understood by using the Froude number, Fr , where $Fr = U_a / C$, where U_a is the speed of the atmospheric disturbance and C is the shallow water wave celerity. Maximum resonance occurs as the Froude number approaches 1. The third requirement for meteotsunami generation is that the resonant atmospheric disturbance propagates toward a semi-enclosed basin, such as a harbor. This requirement, however, was challenged by showing that a strong convective system propagating seaward could cause a wave that reflected off the shelf, back toward the coast [Sepić and Rabinovich, 2012]. Lastly, in order for a meteotsunami to demonstrate devastating effects, embayment resonance must occur, where the period of the incoming meteotsunami matches the resonant period of the associated embayment.

In 2004, de Jong and Battjes found that meteotsunami generation is more sensitive to wind oscillations associated with convective systems than to a moving atmospheric pressure disturbance. These results were shown in the North Sea when analyzing low-frequency waves in vicinity of Port of Rotterdam, Netherlands. Convective systems exist when a cold front moves over an area of warm water, causing an unstable lower atmosphere. This causes warm air at the sea surface to ascend. Movement of warm air into the atmosphere draws air underneath these convective cells to fill the void. If the air is sufficiently moist,

condensation can cause a release of latent heat that increases the rate of airflow. Narrow bands of clouds occur in these areas of convection, which correspond to areas of precipitation and are visible on radar reflectivity imagery.

The northeastern Gulf of Mexico has recently received attention as a region of meteotsunami genesis [Olabarrieta et al., 2016] because of its shelf-like bathymetry and propensity for cyclogenesis activity. The frequent west to east propagation of storm systems in the northeastern Gulf of Mexico during winter favors the incidence of meteotsunami events at the coast. Increased incidence of meteotsunamis seems to coincide with El Niño episodes. This correlation motivated the exploration of meteotsunami incidence during the 2015-2016 El Niño. The purpose of this study is to analyze the role of atmospheric forcing on meteotsunami generation and to characterize the spatial structure of meteotsunami waves in the northern Gulf of Mexico. These two objectives were achieved with a series of water level and atmospheric measurements along the northwestern coast of Florida, between Pensacola and Apalachicola Bays.

CHAPTER 2 METHODS

Water level data were obtained from December 2015 to February 2016 at 3 CTD locations (P1, P3 and P4; P2 was not recovered) and 4 NOAA stations (Figure 2-1). A CTD-Diver instrument recorded conductivity, temperature, and depth every 2 minutes. Station P1 was located approximately 10 kilometers east of the Destin inlet, P3 was approximately 5 kilometers east of the Panama City inlet, and P4 was located approximately mid-way between Panama City Beach and Port St. Joe. NOAA stations at Pensacola (PSC), Panama City Beach (PCB), Panama City (PC) and Apalachicola (ALC) provided water level, barometric pressure, wind, and temperature data at 6-minute intervals.

All CTD and NOAA water level signals were first de-tided using the U-Tide program [Codiga, 2011]. Once the tidal signal was removed, a band-pass PL66TN filter was applied with a window period of 0.25-6 hours to remove other low frequency oscillations and high frequency contributions from wind waves. The signals at PCL, PCB, PC, and ALC were then linearly interpolated to provide 2 minute interval spacing to match the CTD records. The threshold to identify meteotsunamis was a value of 5 standard deviations (5σ) from the mean filtered records. This threshold was higher than that suggested by Monserrat et al, 2006 but lower than the threshold of 6σ suggested by Olabarietta et al, 2016. Next, an amplitude threshold was established of 30cm (e.g. Rabinovich and Monserrat, 1996), to clearly separate a meteotsunami signal from the inverse barometer effect. This ensured that spurious meteotsunami signals were not included in the data analysis. Once these metrics were applied to all water level records, events

were identified coinciding at 3 or more sites. This allowed for description of the progression of movement of water level fluctuations in a meteotsunami event.

Each of the 4 NOAA signals was high-pass filtered with a PL66TN filter using a cutoff period of 6 hours to remove low frequency oscillations. Unlike the water level signals, the high frequency atmospheric pressure signal was preserved to compare the role of isolated pressure jumps to that of atmospheric gravity waves. In reality, this analysis was limited due to the 6-minute sampling period.

Morlet Continuous Wavelet Transform analysis was performed on the de-tided, filtered water levels to show the structure of the meteotsunami signal in the frequency domain and how that structure changed over time [Morlet et al., 1982]. The same analysis was used on the filtered atmospheric pressure records to determine if the frequency structure of the water level and atmospheric pressure were related. Additionally, low-frequency wind variations associated with convective systems have been shown to affect meteotsunami growth [de Jong and Battjes, 2004]. Using wind data provided by the NOAA buoys at PCB and ALC, continuous wavelet transform analysis was used to determine the frequency structure of these low-frequency wind oscillations.

A 100m-resolution grid of the Gulf of Mexico coastline was obtained from NOAA, along with a 0.05° resolution bathymetry grid. Additionally, radar reflectivity images were obtained from the NOAA Level III NEXRAD database. The speed and direction of the atmospheric disturbance associated with each

event was determined with vector addition, assuming that the atmospheric disturbance moved as a plane wave at a constant speed.

Because meteotsunamis are a product of resonance, a Froude number analysis was conducted to determine the potential location of this resonance. As discussed in Chapter 1, meteotsunamis have periods ranging from minutes to hours and, as such, always behave as shallow water waves in the coastal region [Monserrat et al, 2006]. Using the shallow water wave celerity approximation of $C = \sqrt{gh}$, where C is the shallow water wave celerity, g is the gravitational acceleration and h is the local water depth, one can see that meteotsunami wave speed is a function of depth. With this in mind, the bathymetry mentioned above was used to create a spatial representation of the Froude number for each event.



Figure 2-1: Locations providing data for this study. NOAA sites are shown as red triangles and CTD locations are shown as red circles. Henceforth, Pensacola will be referred to as PSC, Panama City Beach will be referred to as PCB, Panama City will be referred to as PC, and Apalachicola will be referred to as ALC.

CHAPTER 3 RESULTS

Using the metrics described in Chapter 2, three meteotsunami events were identified between December 14, 2015 and February 16, 2016. Figure 3-1 shows the water level signal at all 7 stations for each of these three events. Of note, stations Pensacola, Panama City, and Apalachicola demonstrate damped meteotsunami signals because they are located inside estuaries. The third event, February 16th, occurred as the instruments began to cease recording, resulting in incomplete data for that event. This also prevented analysis of the frequency signal using a Morlet Wavelet due to the cone-of-influence collapsing. As such, the event on February 16th, 2016 is not analyzed further in this paper.

January 15, 2016

On January 15, 2016 a meso-scale convective system (MCS) developed in the northwest Gulf of Mexico. As is common with most winter storms in this area, the storm had a general west to east propagation. The radar reflectivity imagery can be seen in Figure 3-2 a-c. The associated atmospheric pressure signal, obtained from stations PCB and ALC, is shown in Figure 3-2.d and 3-2.e. Both signals are high-pass filtered with a 6-hour cutoff period. As the system passed over stations PCL and P1, no clear squall line was yet present. At about 0730, a north-south squall line began to emerge over Panama City with an apparent west to east propagation. The intensity of this squall line continued to increase as the storm moved eastward, resulting in a maximum intensity over ALC. As it passed over station PCB, the system showed a maximum pressure change of ~3.5 hPa over ~36 mins. The pressure change also occurred in the

form of an oscillatory motion, instead of the often-cited instantaneous jump in meteotsunami generation [Choi et al, 2008]. As the atmospheric system developed and passed over ALC, it then displayed a maximum pressure change of ~4 hPa over ~36 mins. The nature of the pressure change at ALC is characteristic of an abrupt pressure change, typically associated with a well-developed squall line. When standardized over a 10-minute interval the values for pressure change at PCB and ALC were 0.97 hPa/10mins and 1.11 hPa/10mins, respectively.

As seen in Figure 3-3, the first station to show a water level signal meeting the criteria for a meteotsunami event (5 sigma or greater and at least 30 cm in height) was P3 at ~1006 UTC with a wave height of ~30 cm. The next station was P4 at ~1032 UTC with a wave height of ~74 cm. The third and final station to demonstrate the characteristics of a meteotsunami was PCB at ~1124 UTC with a wave height of ~32 cm. Fluctuations are visible at each of the other four stations but do not meet the criteria for a meteotsunami event and are not considered in data analysis moving forward.

To better understand the relationship between the behavior of an atmospheric disturbance and sea level response, a simple comparison of atmospheric pressure and water level is insufficient. Continuous Wavelet Transform analysis was conducted on both the atmospheric pressure signal and the water level signal at each of these 3 applicable stations. The results of these analyses are shown in Figure 3-4. When comparing the atmospheric pressure signal at PCB to the signal at ALC, the general frequency structure of the signal

changed little as the system propagated from one location to the other. At PCB, maximum energy occurred with a period of ~2.2 hours at ~1000 UTC. At ALC, maximum energy occurred with a period of ~2 hours at approximately 1030 UTC. As seen in Figure 3-4.d and 3-4.e, the amplitude of the pressure change increased as the system propagated from PCB to ALC and the period associated with maximum energy decreased.

Wavelet analysis of the water level at PCB reveals maximum energy with a period of ~2 hours starting at 1100 UTC and lasting until 1400 UTC. Although the structure of the atmospheric pressure signal and water level signal are similar, there is a time lag of approximately 2 hours that occurred between the two different signals as they arrived at PCB. This time lag suggests that the wave separated from the atmospheric disturbance at some point offshore and slowed due to shoaling. At P3, maximum energy occurred with a period of ~2.2 hours at 1500 UTC. The time lag between maximum energy at PCB and P3 (approximately 5 km apart) suggests that interference, potentially due to refraction, may be masking the first arrival of the wave at P3. Sheremet et al. (2016) showed that constructive interference is possible due to refraction. As such, one can surmise that deconstructive interference is also possible. Whereas the signal at PCB dissipated after a few hours, the signal at P3 continued with similar energy to the leading edge. Occasional peaks of energy can be identified later that day with shorter periods of ~20 minutes, ~60 minutes, and ~100 minutes. Lastly, at P4, a leading edge of high energy appears at 0900 while the signal continued in the range of periods from 0.5 hrs to 2 hrs. This interval of high

energy occurred from 0900 UTC to 1100 UTC, at which point high energy only persisted in the range of 1 hr to 2 hrs until 1300 UTC. Later in the day, intervals of high energy were present in bands at 1 hour periods and 0.5 hour periods while original high energy periods of ~2 hours disappeared.

A relationship is evident between the frequency structure of the atmospheric pressure signal and the frequency structure of the water level signal. Wavelet coherence was used to quantify this relationship, but yielded little to no coherence (results not shown). This lack of coherence suggests that another mechanism during this event leads to meteotsunami generation. De Jong and Battjes (2004) provide a sketch to describe the mechanisms of low-frequency (0.1-2.0 mHz) wind oscillations associated with convective cells as seen in Figure 3-5. The wind records from PCB were analyzed to determine if the behavior of the wind played a role. The high-pass filtered east component of the wind is shown for January 15th in Figure 3-6. Wavelet analysis explored the frequency structure of these wind oscillations (Figure 3-7). The wind frequency structure behaves similarly to both the atmospheric pressure signal and the water level signal, but shows no time lag. In this case, the wavelet coherence (Figure 3-8) between water level and eastward wind is more revealing than the wavelet coherence between water level and atmospheric pressure. Coherence > 0.8 exists at periods between 2 and 4 hours for the duration of the event. The wind signal leads the water level signal by approximately 90-180 degrees, which corresponds to a lead-time of 0.5 to 2 hours.

To quantify the speed and direction of the atmospheric disturbance, a version of vector addition was used. Other methods have been proposed such as the Isochronal Method (Orlić, 1980) and the Cross Correlation Function Method (Monserrat & Thorpe, 1992). The Isochronal Method assumes a plane wave and uses a least squares regression to minimize the difference between expected and calculated atmospheric disturbance propagation. The Cross Correlation Function Method allows for an atmospheric disturbance to be dispersive, meaning that different frequency bands within the system can move in different directions and at different speeds. In this way, one can analyze multiple independent aspects of one storm system and isolate only the frequency band(s) that are needed. A third method exists which uses radar reflectivity to create normal vectors from the line of maximum reflectivity and, using time-lapse imagery, calculates the speed of this line. The applicability of this last method will be challenged in Chapter 4 of this paper.

Using vector addition and assuming that the atmospheric disturbance associated with the MCS on January 15, 2016 traveled as a plane wave at constant speed, it traveled at 18.5 m/s with a direction of 118 °T. As noted before, meteotsunami waves, by virtue of their wavelength, travel as shallow water waves. As such, their celerity is a function of water depth. In order for the Froude number associated with this atmospheric disturbance to equal 1, the shallow water wave celerity must also equal 18.5 m/s, yielding a resonance depth of ~35 m. Using a bathymetry grid of the northern Gulf of Mexico, I identified the 35m isobath and those isobaths that would yield a Froude number

of 0.85 and 1.15. Resonance decreases rapidly outside of +/- 5%, but for a spatial representation and conservative analysis, +/- 15% was used [Proudman, 1929]. A visual representation of the spatial variation of this event's Froude number is shown in Figure 3-9.

Again, using the assumption of a plane wave without lateral constraints, a vector indicating the propagation direction can be applied to the spatial representation of the Froude number. This allowed elucidation of the maximum distance at which resonance would occur and the point at which resonance would cease. Upon resonant cessation, the resulting wave would become free. Based on this analysis, the maximum distance that resonance could have occurred during the January 15th event is 88 km. The wave then must have separated from the atmospheric disturbance at a location just south of the Panama City Inlet. At this point, it became free to propagate in the same direction as the atmospheric disturbance before undergoing refraction and shoaling effects.

January 17, 2016

Two days after the January 15 event, a similar event occurred in which a MCS passed over the northeastern section of the Gulf of Mexico from west to east. Figure 3-10 a-c shows the radar reflectivity images for this system. The associated atmospheric pressure signal, obtained from stations PCB and ALC, is shown in Figure 3-10.d and Figure 3-10.e.

In contrast to the January 15th event, this system did not appear to have a well-developed squall line associated with it. Rather, it contained a swath of radar reflectivity values that were more uniform than on January 15th. This poses a

challenge when attempting to locate the section of the system in which an atmospheric pressure disturbance would exist (typically one can assume it exists at the squall line). Although no such line is visible, the magnitude of pressure change is greater at both PCB and ALC than on January 15th. The maximum pressure change at PCB is 4.2 hPa in ~24 mins while the maximum pressure change at ALC is 4 hPa in ~42 mins. When standardized over a 10-minute interval, these pressure changes at PCB and ACL equate to 1.75 hPa/10mins and 0.95 hPa/10mins, respectively. Comparing this to the event on January 15th, the rate of pressure change is 56% higher at PCB while the rate of pressure change at ACL is 14% lower on January 17th than it was on January 15th. This analysis demonstrates a weakening of the pressure disturbance as it propagates eastward, in contrast with the January 15th atmospheric disturbance, which strengthened over time. Also of note, the initial N-wave structure of the atmospheric pressure signal at PCB changes to a nearly solitary atmospheric pressure signal at ALC. This unique behavior may affect the resonance process for meteotsunami generation, but has not been simulated in numerical models. The trough of the atmospheric pressure signal is eliminated as it passes over ALC, suggesting that multiple atmospheric pressure signals with different frequencies are moving within the system at different speeds, causing constructive or destructive interference. This behavior has been shown to exist and is the basis for the Isochronal Method for quantifying the speed and direction of atmospheric disturbances [Orlić, 1980].

On January 17th, the first station meeting the aforementioned criteria for water level signal was P1 (as measured at time of peak water level) at 0850 UTC with a wave height of ~38 cm. The signal then appeared to propagate eastward from this location. The next station to show maximum wave height was PCB at 0928 UTC with a wave height of ~33 cm. Following PCB were P3 and P4 which exhibited the signal simultaneously with wave heights of ~44 cm and ~60 cm, respectively. The January 17th water levels are shown in Figure 3-11.

As was the case on January 15th, a wavelet analysis was conducted on both the atmospheric pressure signal and water level signal associated with the January 17th event. These analyses are shown in Figure 3-12 a-e. The frequency structure of the atmospheric pressure signal at PCB shows an initial high energy band arriving at approximately 0400 UTC with a dominant period of ~2 hours. By 0800 UTC, this structure has changed to a maximum energy contribution from a dominant period of ~2.5 hours but notably higher energies across the energy spectrum from ~10 minutes to ~3 hours. By ~1800 UTC, all energies above the 95% confidence limit have dissipated. The ALC structure is similar in that it also shows an initial high-energy contribution from a period of ~2 hours, occurring at approximately 0600 UTC. This main contribution from a period of ~2 hours persists until approximately 1000 UTC, where it then dissipates.

Wavelet analyses of the water levels at PCB, P3, and P4 (shown in Figure 3-12 c-e) tell a similar story. Most notably, the water level frequency structure at PCB shows a leading edge of high energy at approximately 0600 UTC with a dominant period of ~2.5 hours, followed shortly thereafter by a relatively uniform

distribution of high energy from periods of 1 hour to 2.5 hours. Moreover, a simple visual comparison between the two shows a remarkably similar structure between the atmospheric pressure signal and water level signal at PCB. At P3, wavelet analysis of the water level signal shows a similar overall structure to PCB, but identifying a leading edge of high energy is difficult due to the spread of high energies over different frequencies. The maximum energy at P3 occurs at approximately 1000 UTC with a dominant period of ~2.5 hours. Lastly, at P4, water level wavelet analysis shows higher energies across the entire time window, with maximum energy occurring at approximately 0800 UTC with dominant periods of ~1.2 hours and ~2.5 hours. By 1500 UTC, these high-energy bands have dissipated into lower energy, broad-spectrum contributions.

The high-pass filtered wind signal, shown in Figure 3-13, reveals oscillatory motion with smaller amplitudes than on January 15th. When converted into frequency space, one can see that the frequency structure of the wind oscillations does not appear in sync with the water level or atmospheric pressure signal (Figure 3-14). Maximum energy occurs at ~0600 with a period close to 3 hours. From here, no discernable behavior exists. Wavelet coherence was then used to quantitatively analyze the relationship (or lack thereof) between water level and wind oscillations. The result, shown in Figure 3-15, is somewhat surprising and shows significant coherence ($>.8$) in periods between 1.5 and 2.5 hours for the duration of the event. The wind signal leads the water level signal by $\sim 135^\circ$, also corresponding to a lead-time of between 0.5 and 1 hour. Just as was shown in the January 15th analysis, the role of wind oscillations cannot be

neglected in studying the relationship between meteotsunami waves and atmospheric forcing.

Applying the same method used to analyze the January 15th atmospheric disturbance speed and direction, the January 17th system moved at 35.6 m/s with a direction of 113.5 °T. For resonance to occur, this atmospheric disturbance speed corresponds to a resonance depth of ~100 m. As before, the 100 m isobath was identified and is shown as a spatial representation of the Froude number in Figure 3-16.

This event produced a free wave just south of P1. While the January 15th event did not produce a signal at P1 meeting meteotsunami criteria, the January 17th system did. This is expected due to the wave becoming free at a more westward location than the January 15th system.

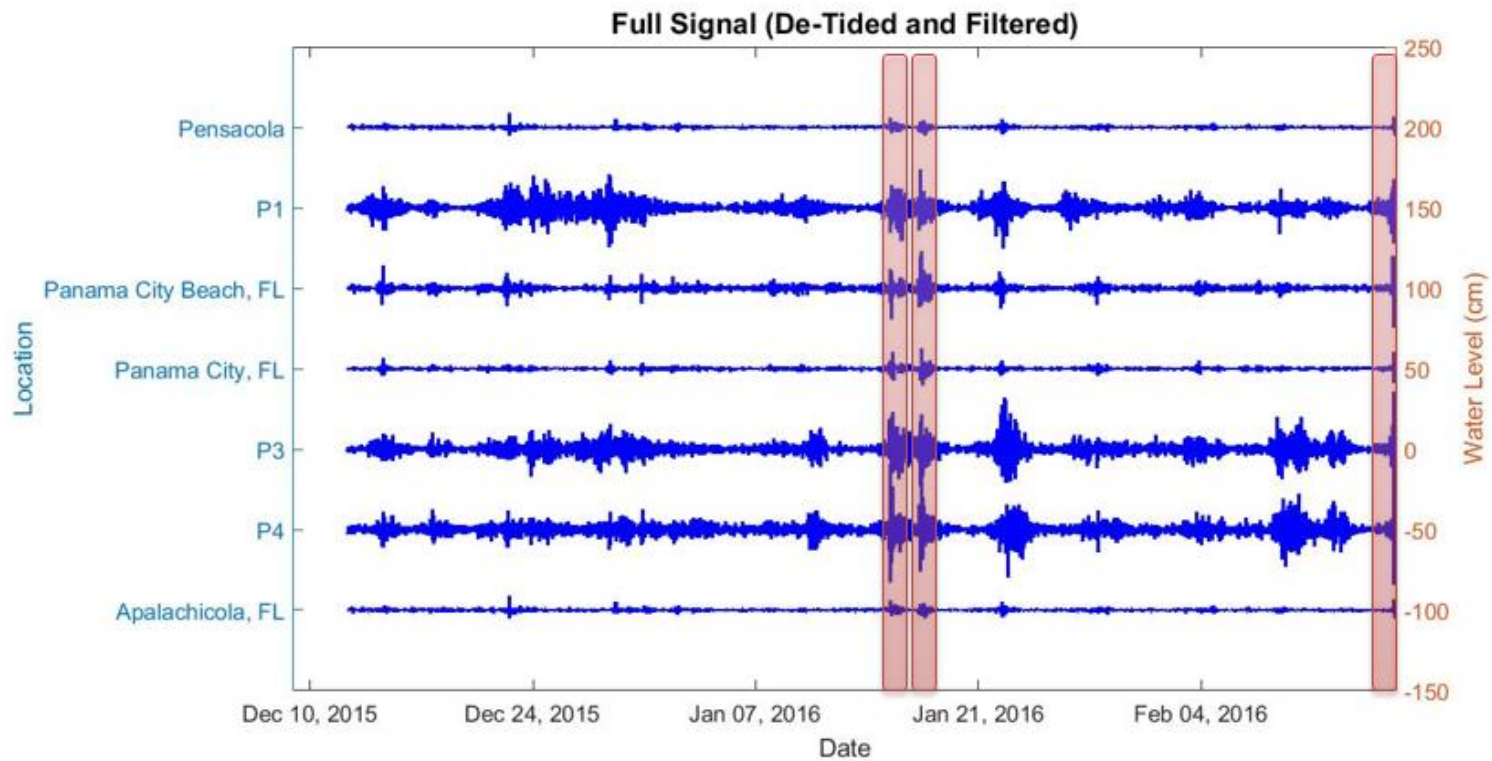


Figure 3-1: De-tided, filtered signal at 7 stations. Wave heights are offset by multiples of 50 cm. The stations are in order from west to east, such that a signal propagating to the right as the y-axis decreases represents an eastward propagation. The events of January 15, January 17, and February 16 are highlighted in red.

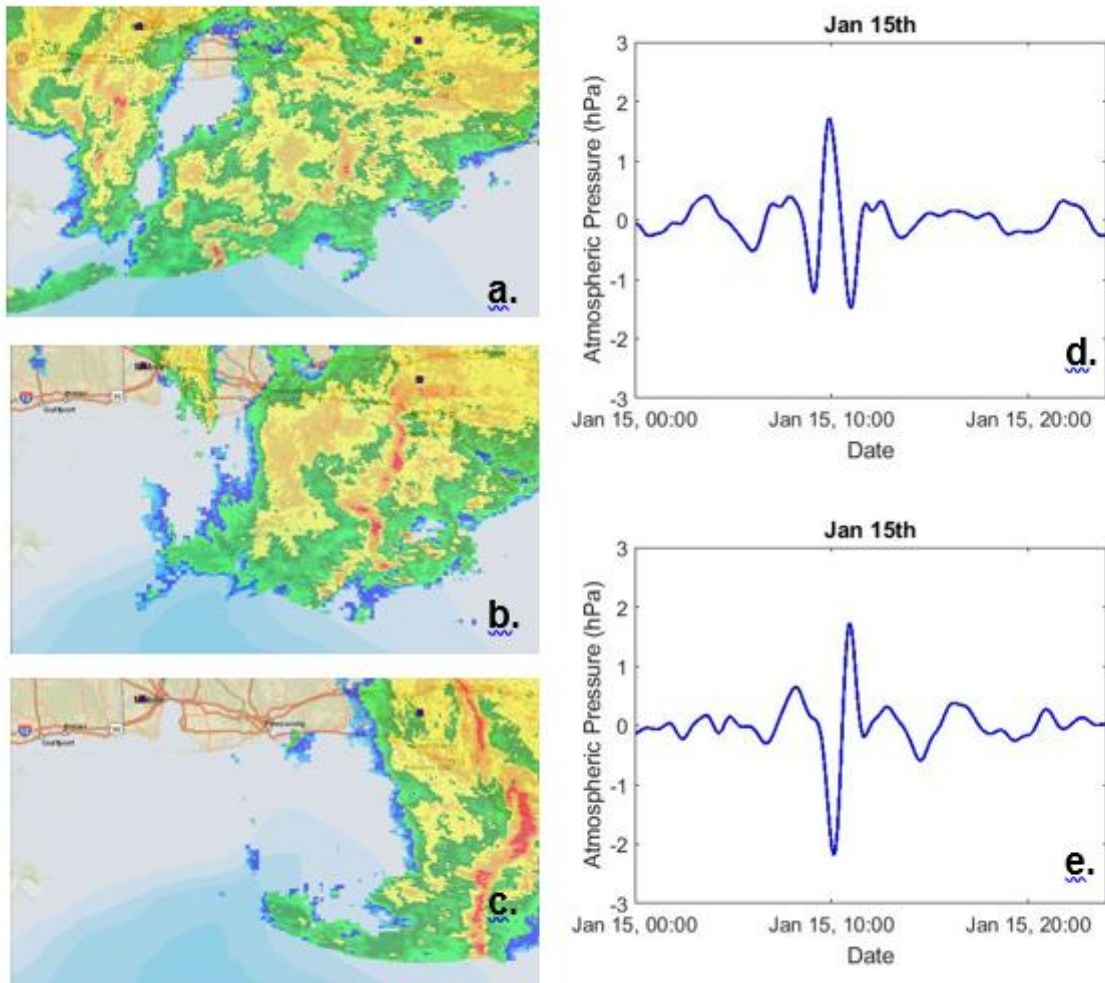


Figure 3-2: Atmospheric conditions on January 15th, 2016. Radar reflectivity imagery from NOAA Level III NEXRAD at a) 0730 UTC, b) 0900 UTC, and c) 1030 UTC. d) High-passed atmospheric pressure signal at PCB and e) high-passed atmospheric pressure signal at ALC.

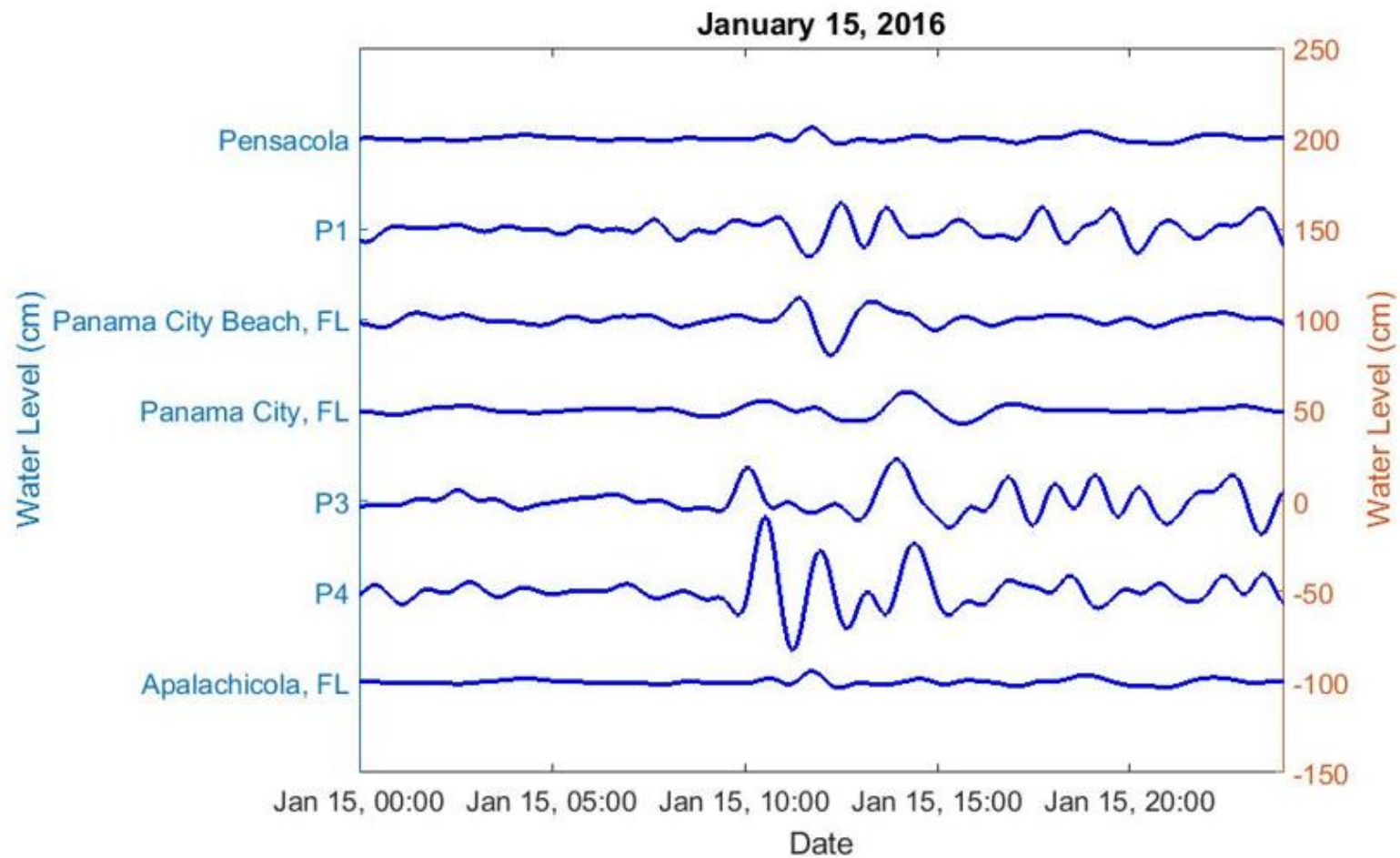


Figure 3-3: Meteotsunami signal on January 15, 2016. Data has been de-tided and band-pass filtered with a window of 0.25-6 hrs.

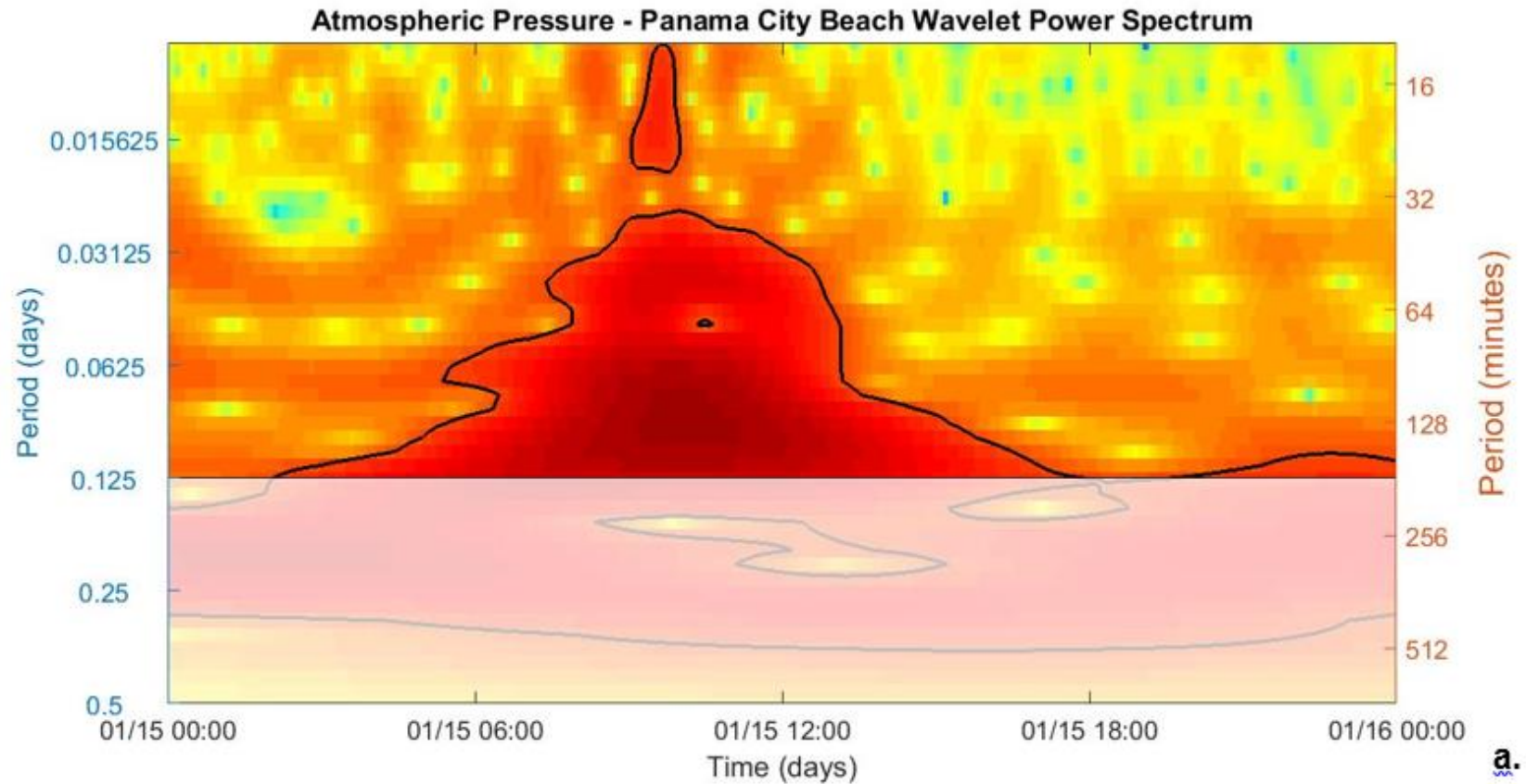


Figure 3-4: January 15, 2016 wavelet analysis of a) atmospheric pressure signal from PCB, b) atmospheric pressure signal from ALC, c) water level signal from PCB, d) water level signal from P3, and e) water level signal from P4. Periods greater than 3 hours have been grayed out to indicate that they are outside of the meteotsunami frequency band.

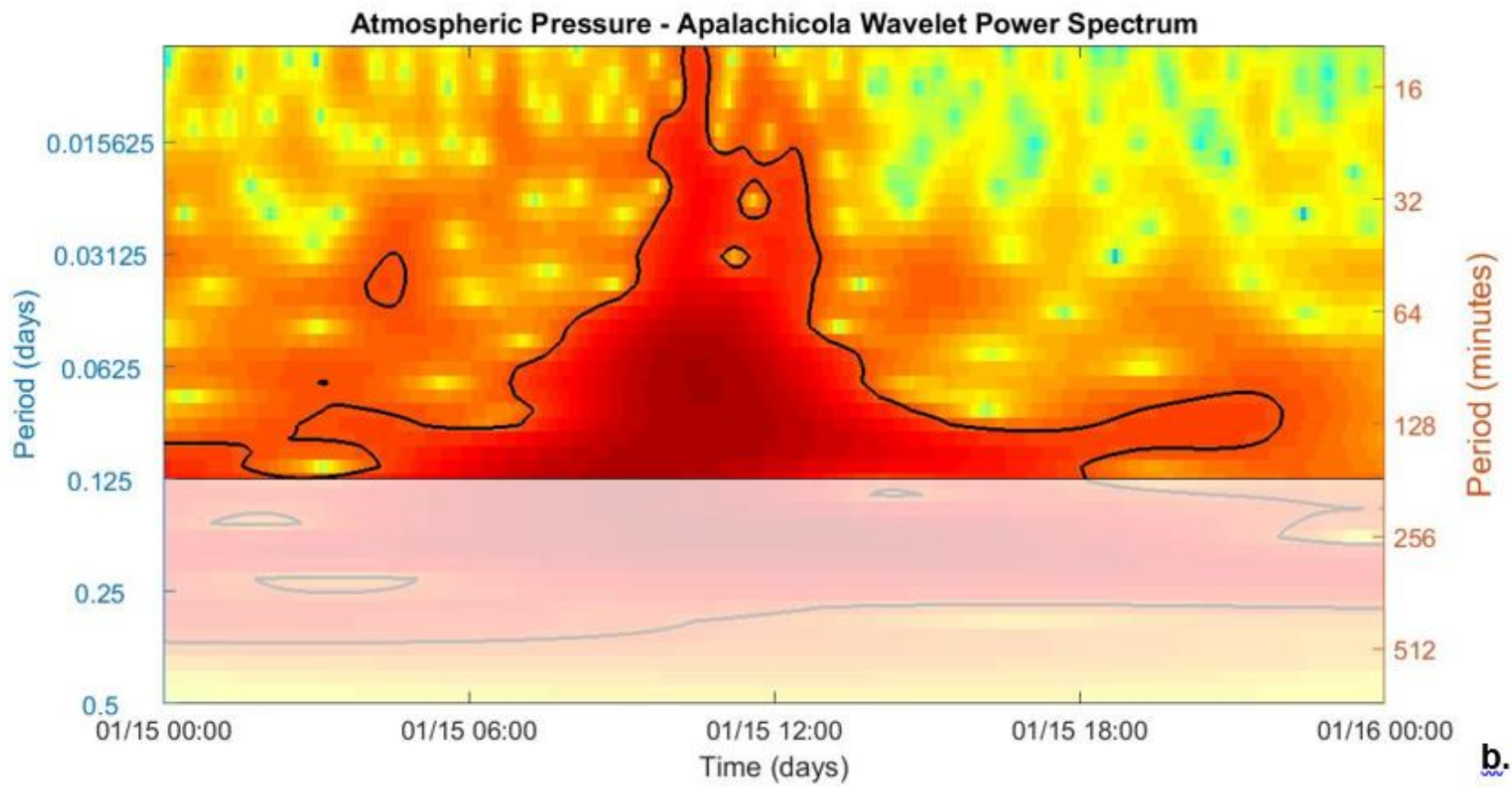


Figure 3-4: Continued

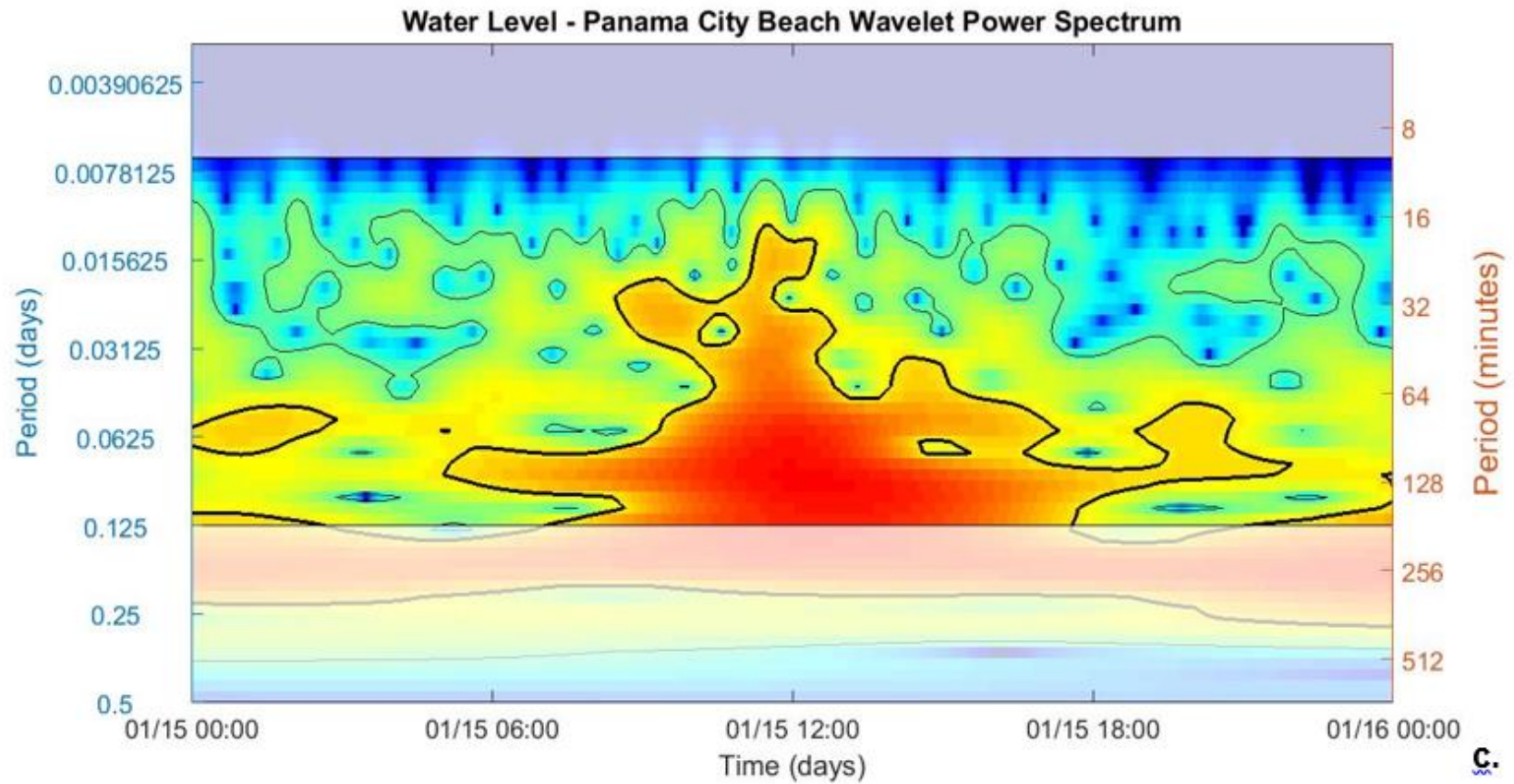


Figure 3-4: Continued

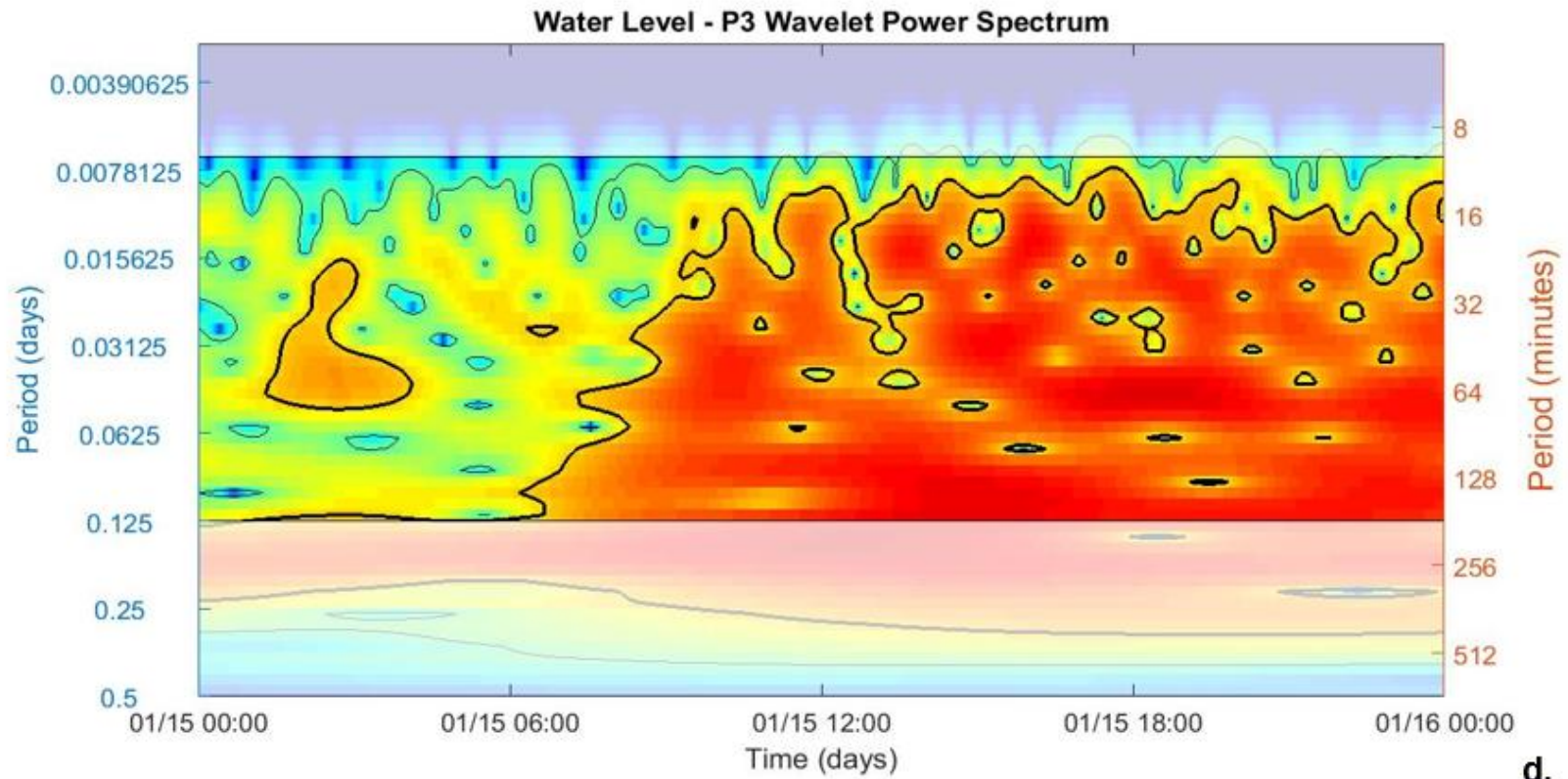


Figure 3-4: Continued

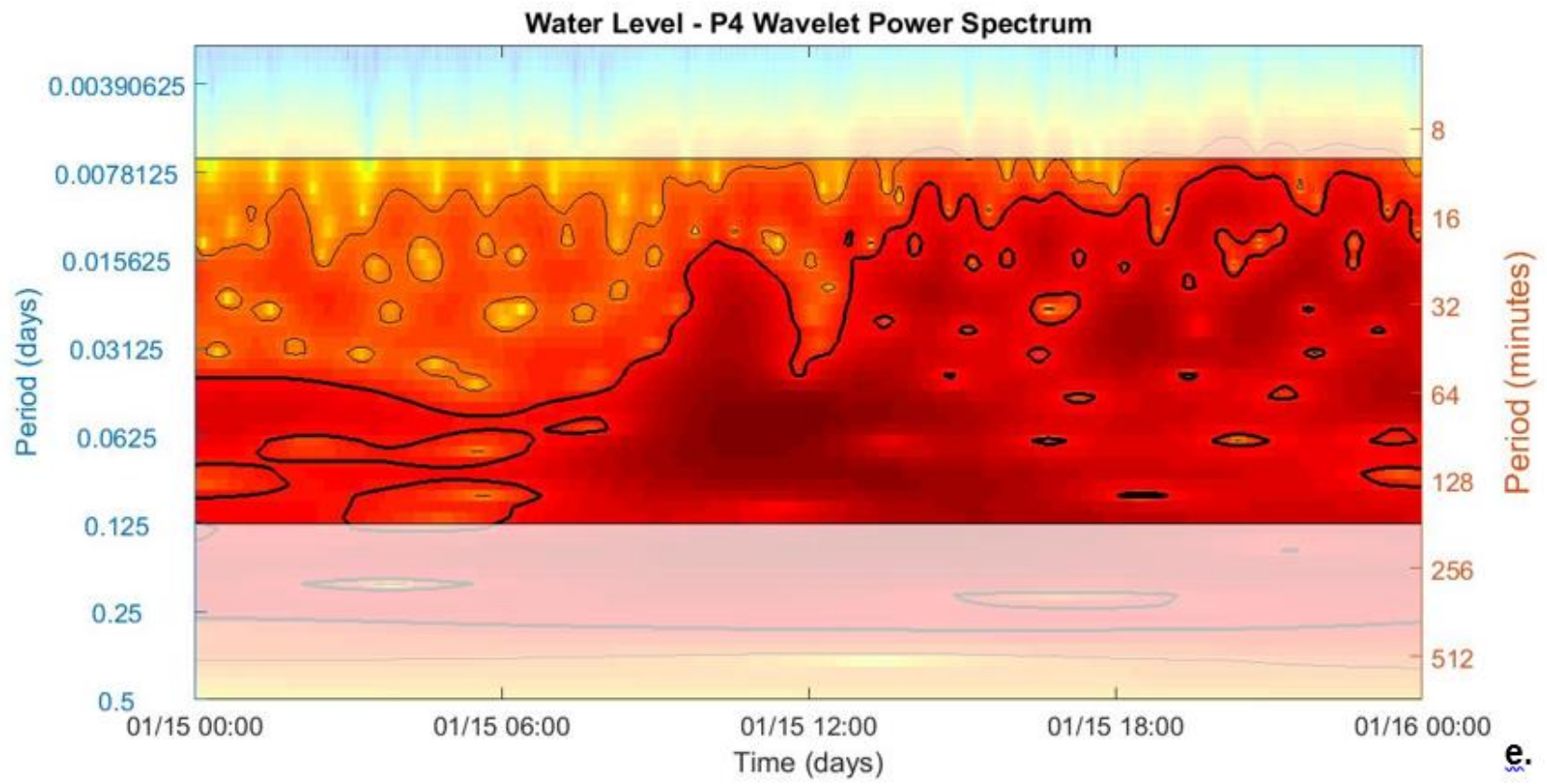


Figure 3-4: Continued

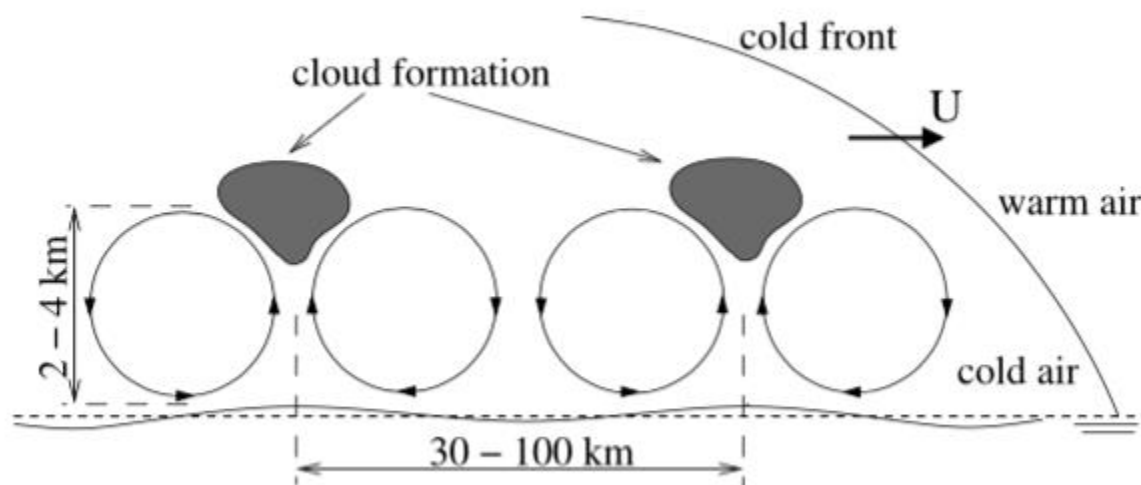


Figure 3-5: Sketch of convection cells in the area behind a cold front together with a theoretical surface elevation response.

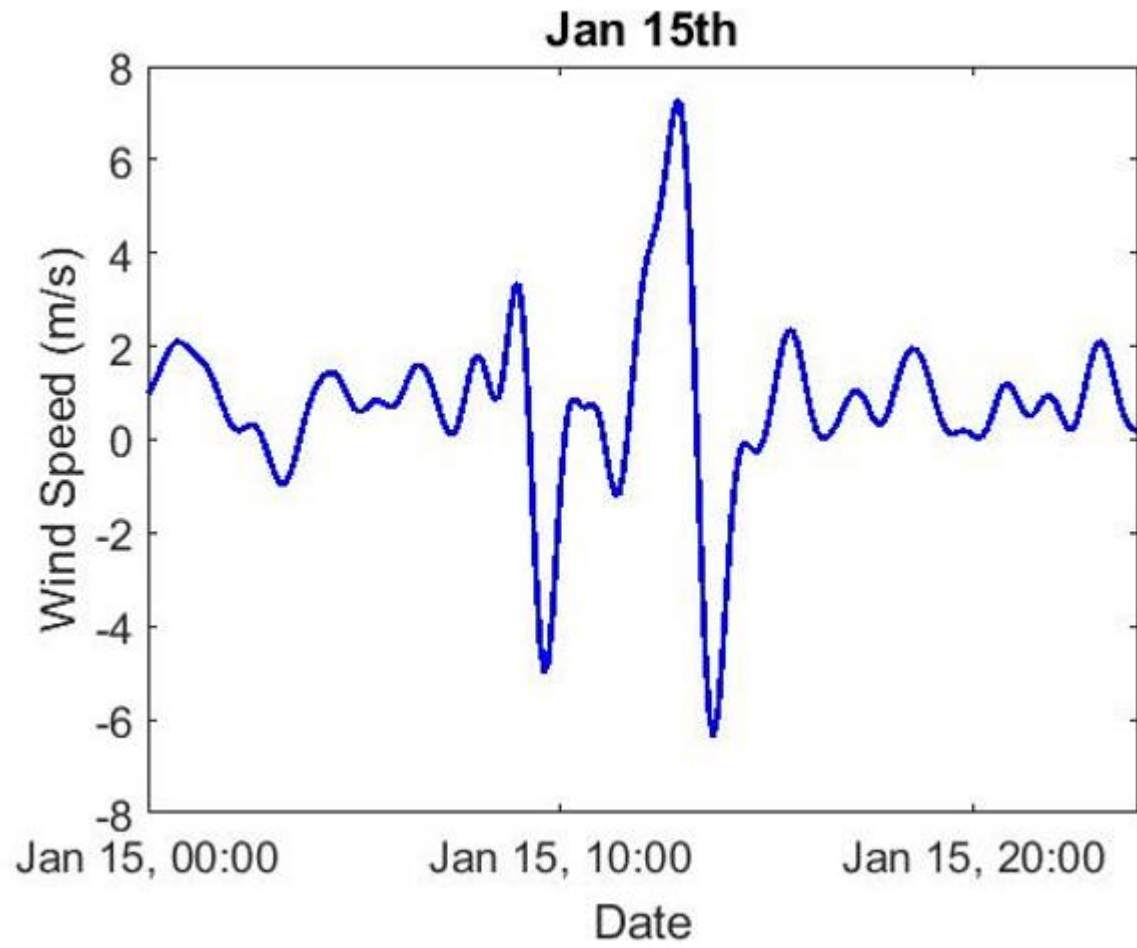


Figure 3-6: Filtered East-West wind record at PCB on January 15th, 2017.

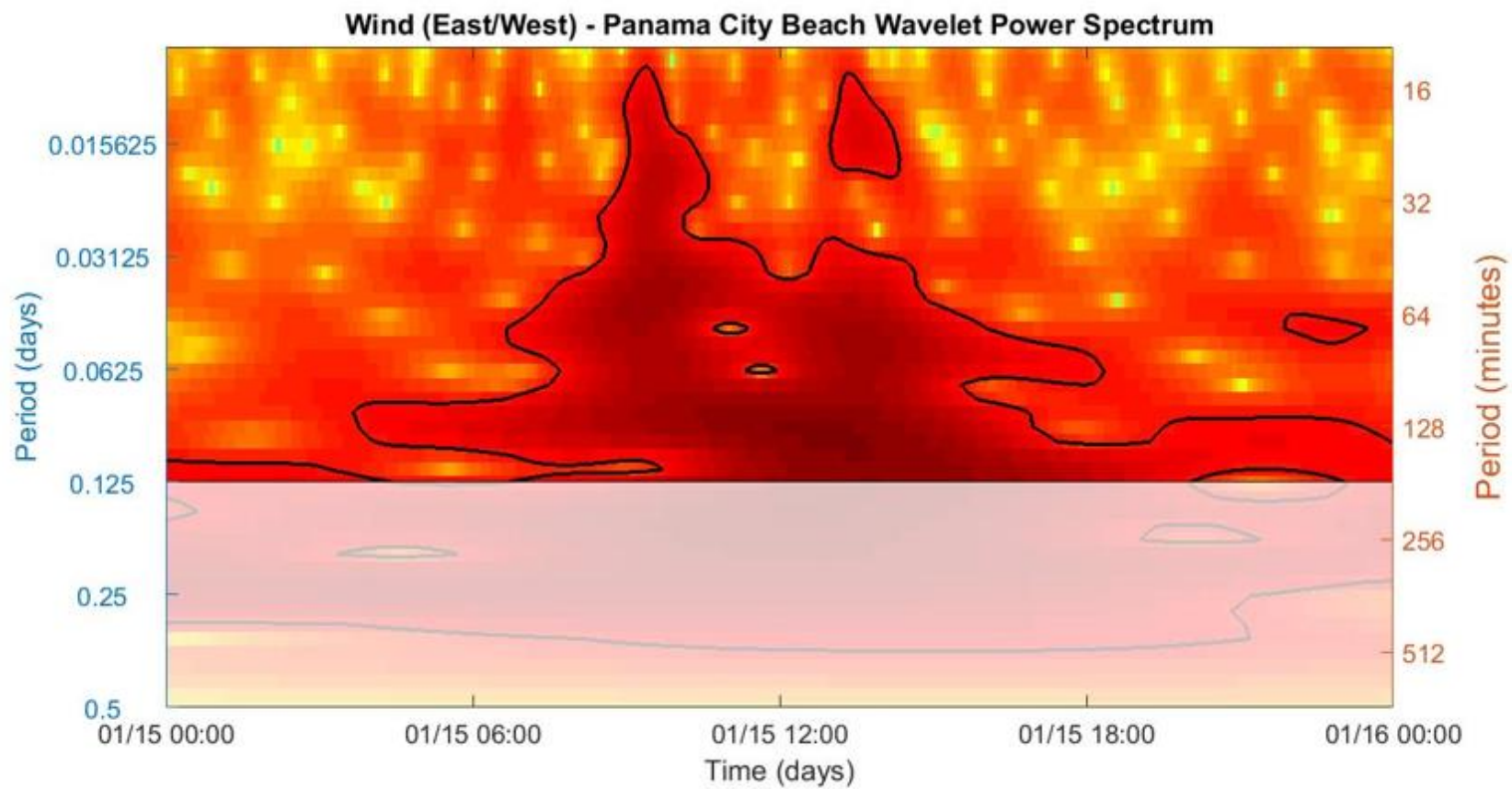


Figure 3-7: Wavelet analysis of wind signal on January 15, 2016 from PCB. Periods greater than 3 hours have been grayed out to indicate that they are outside of the meteotsunami frequency band.

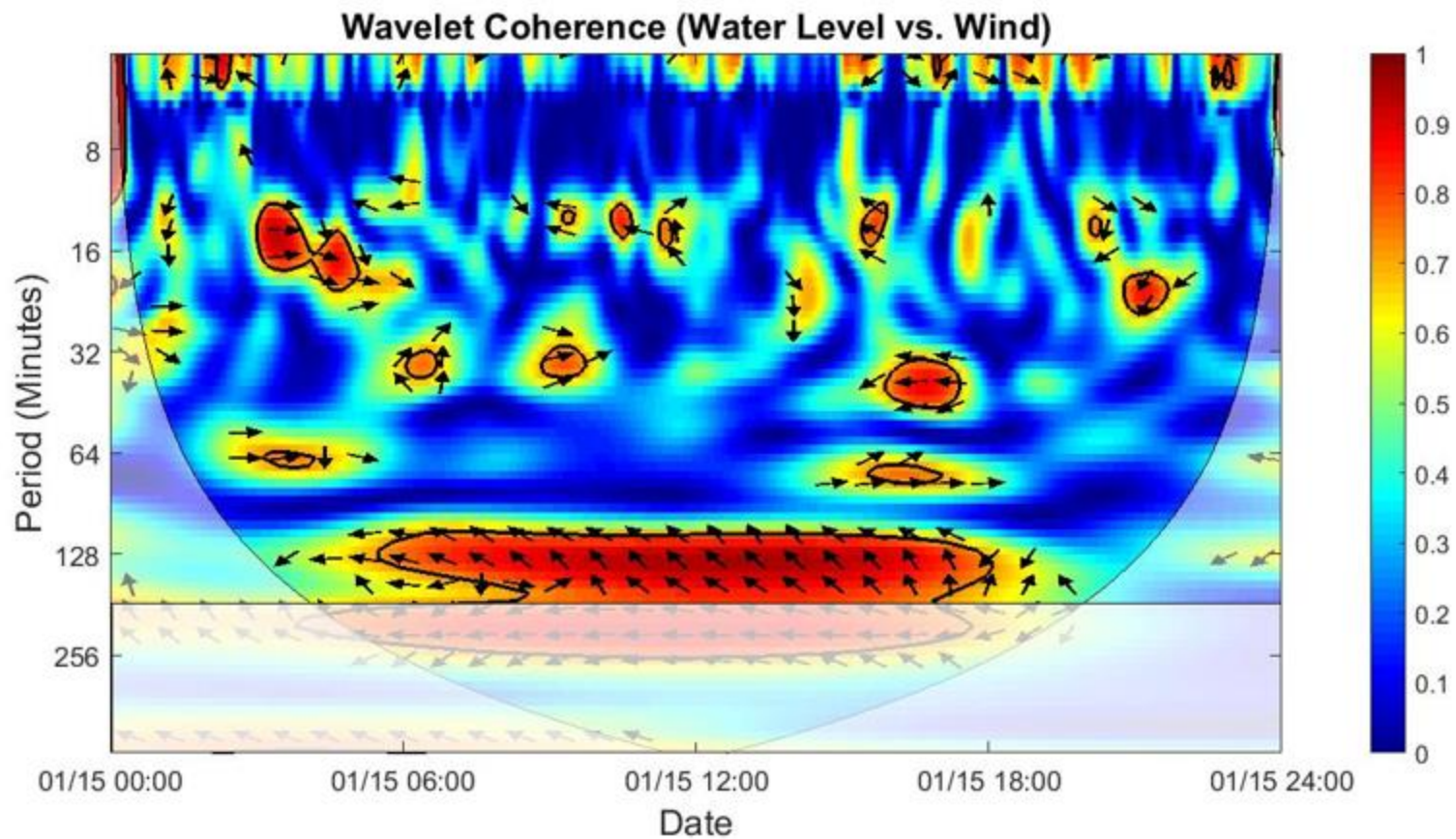


Figure 3-8: Wavelet coherence analysis of wind signal on January 15, 2016 from PCB. Arrows indicate the phase difference between the two signals. (Arrow pointing up indicates water level leads wind by 90°)

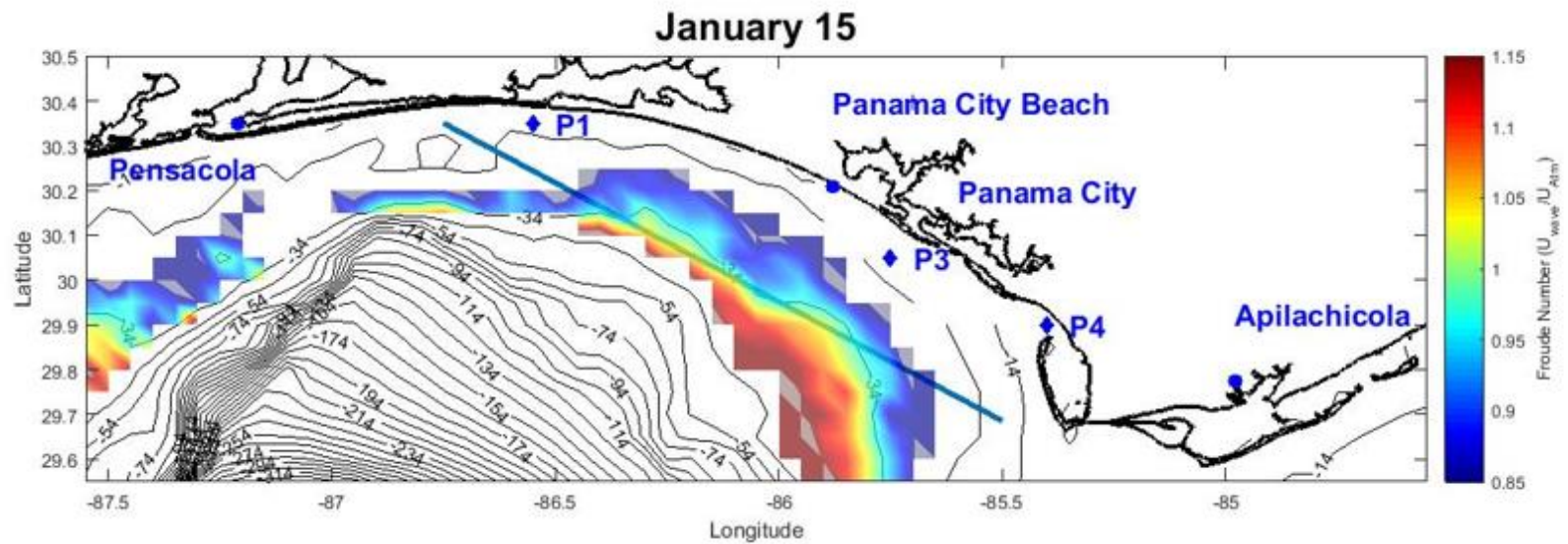


Figure 3-9: Spatial representation of the Froude number for the meso-scale convective system on January 15, 2016. The blue line indicates the propagation of the atmospheric disturbance, optimized for the maximum potential resonance.

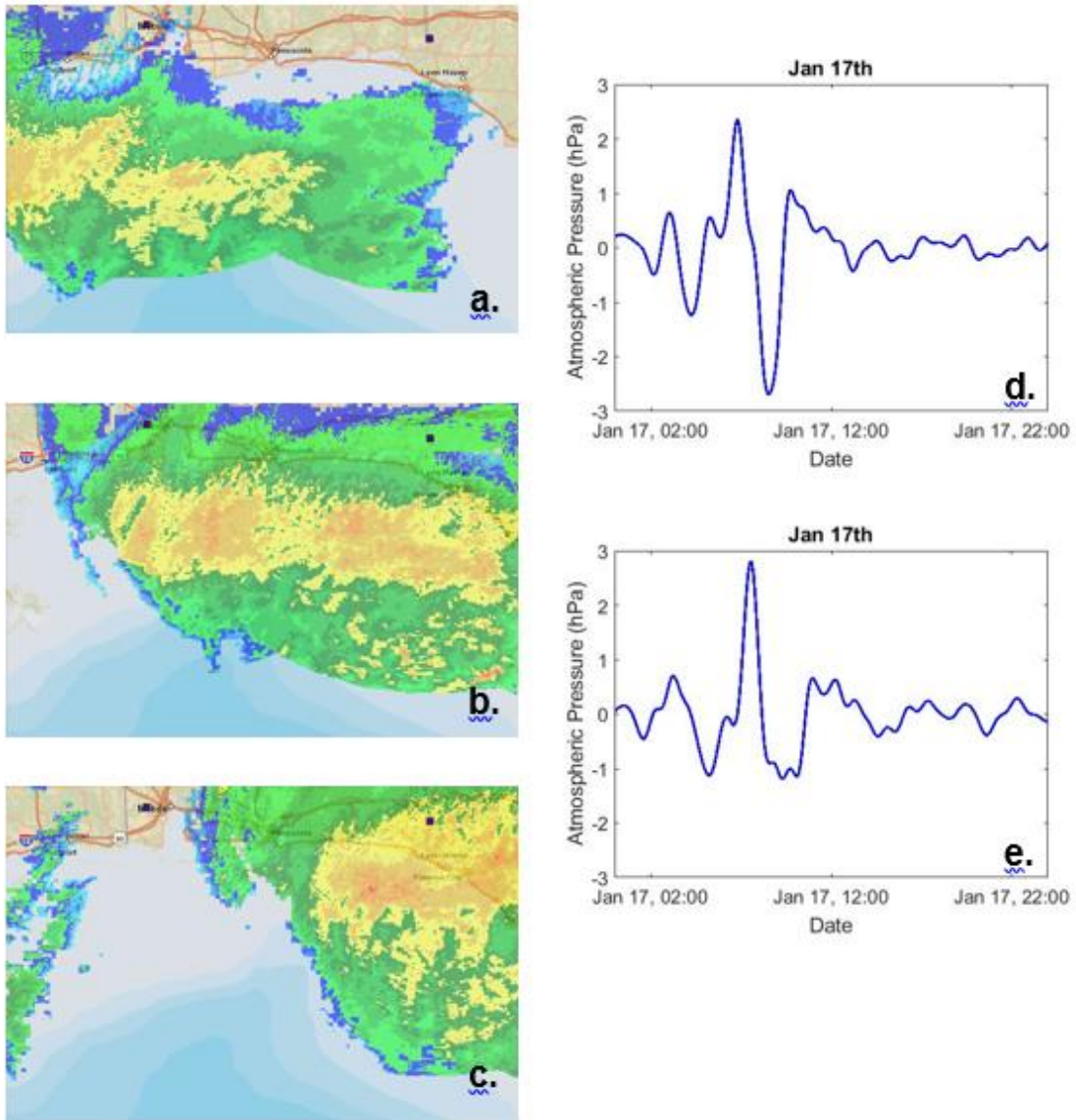


Figure 3-10: Atmospheric conditions on January 17th, 2016. Radar reflectivity imagery from NOAA Level III NEXRAD at a) 0730 UTC, b) 0900 UTC, and c) 1030 UTC. d) High-passed atmospheric pressure signal at PCB and e) high-passed atmospheric pressure signal at ALC.

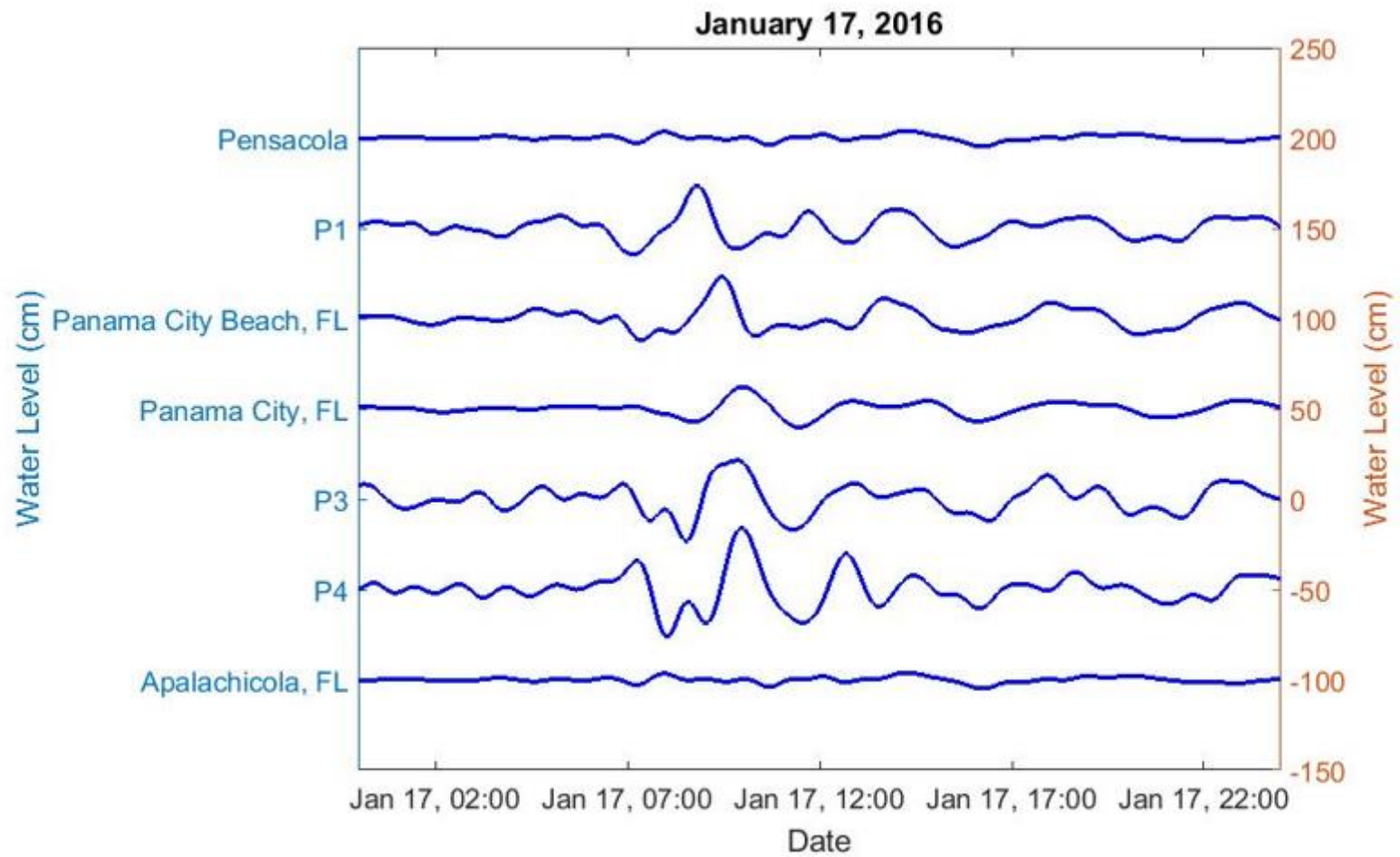


Figure 3-11: Meteotsunami signal on January 17, 2016. Data has been de-tided and band-pass filtered with a window of 0.25-6 hrs.

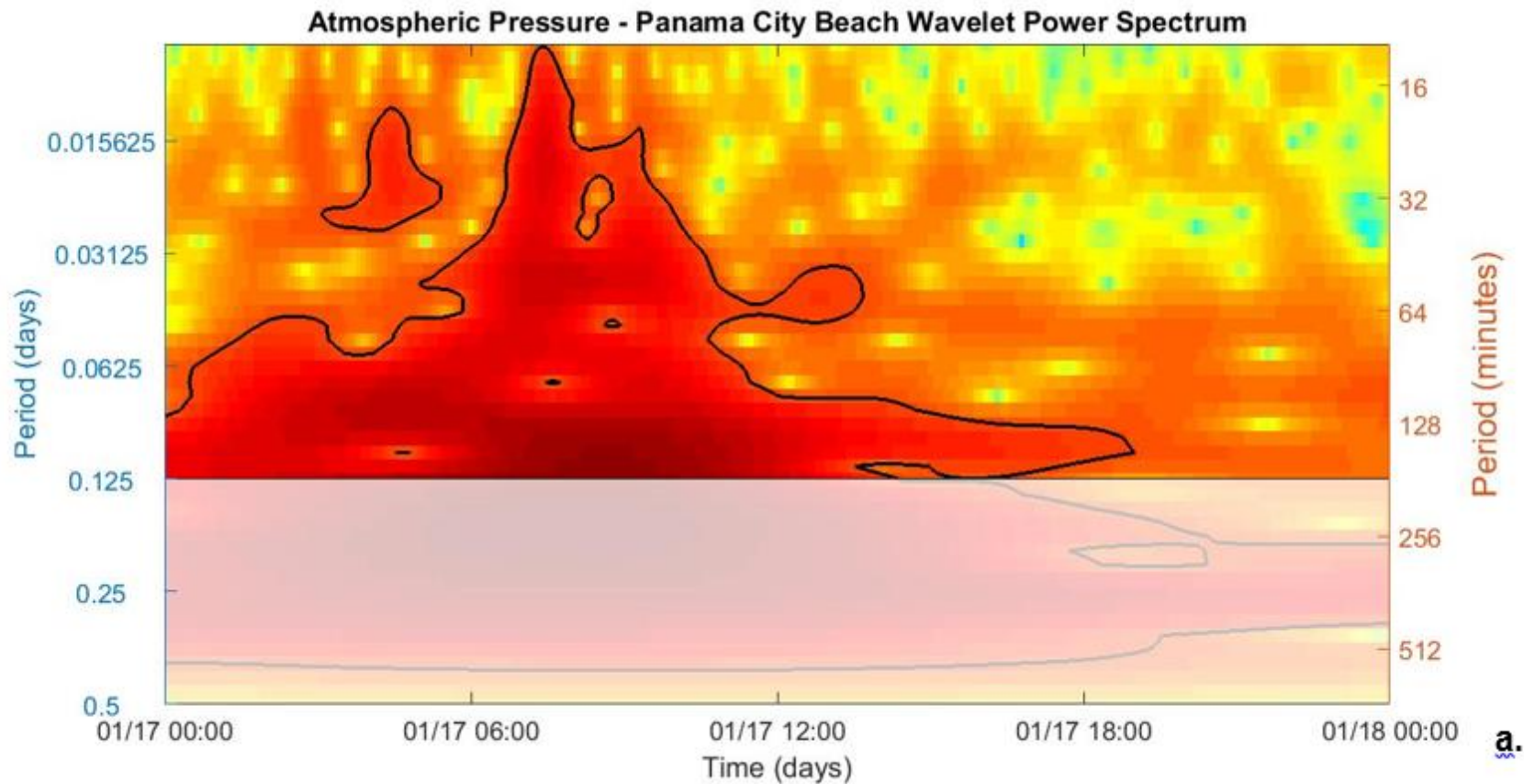


Figure 3-12: January 17, 2016 wavelet analysis of a) atmospheric pressure signal from PCB, b) atmospheric pressure signal from ALC, c) water level signal from PCB, d) water level signal from P3, and e) water level signal from P4. Periods greater than 3 hours have been grayed out to indicate that they are outside of the meteotsunami frequency band.

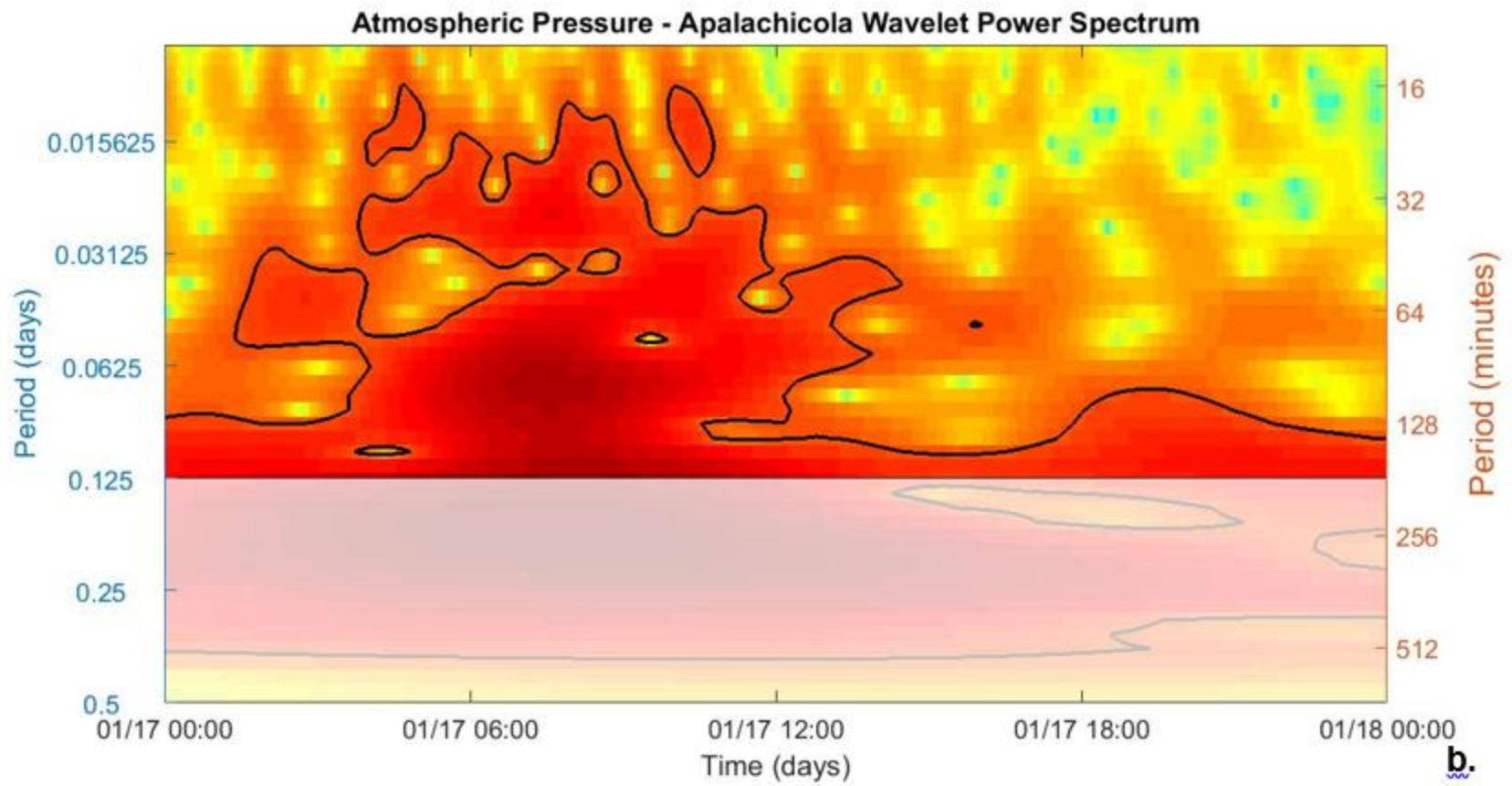


Figure 3-12: Continued

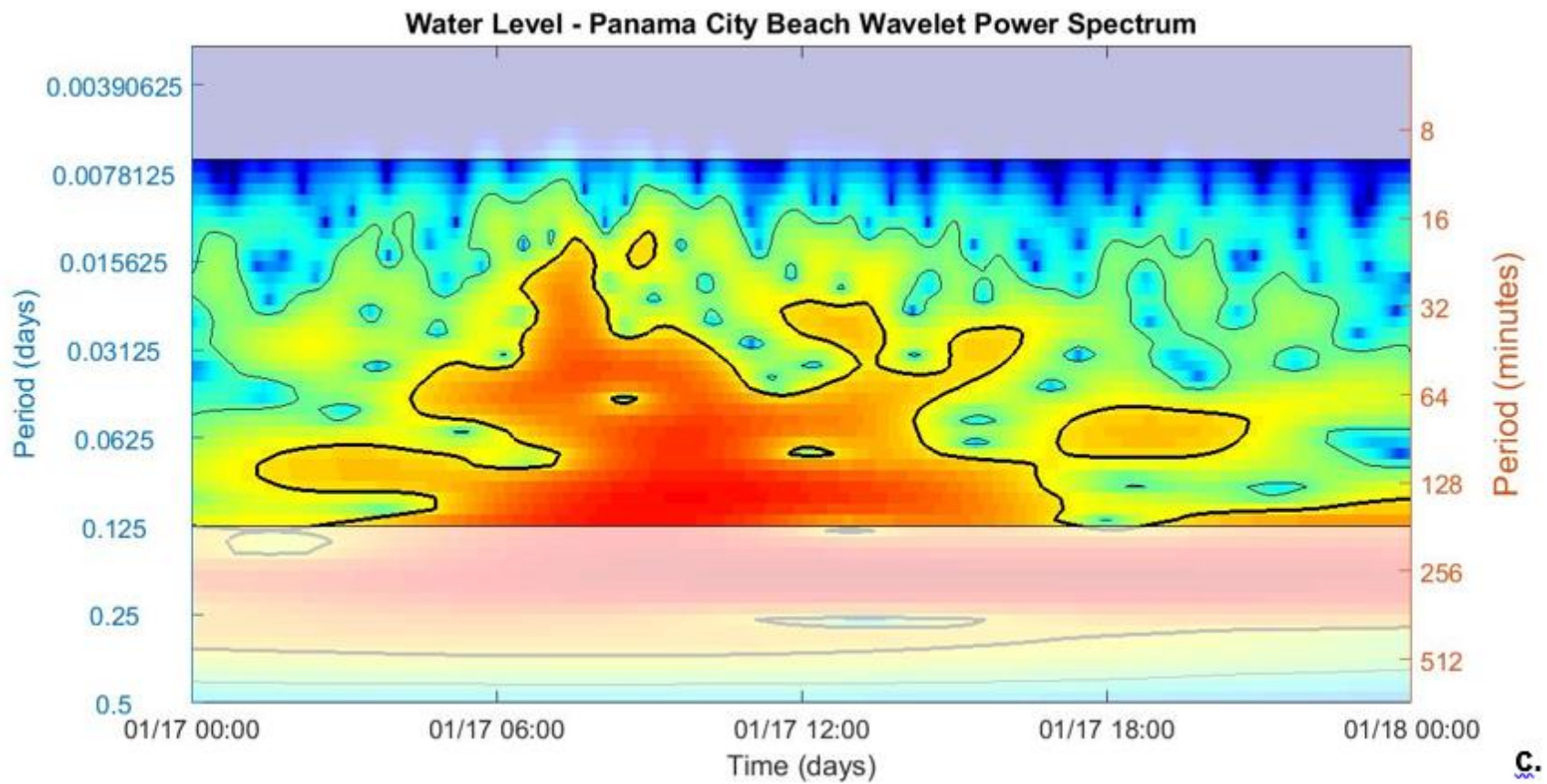


Figure 3-12: Continued

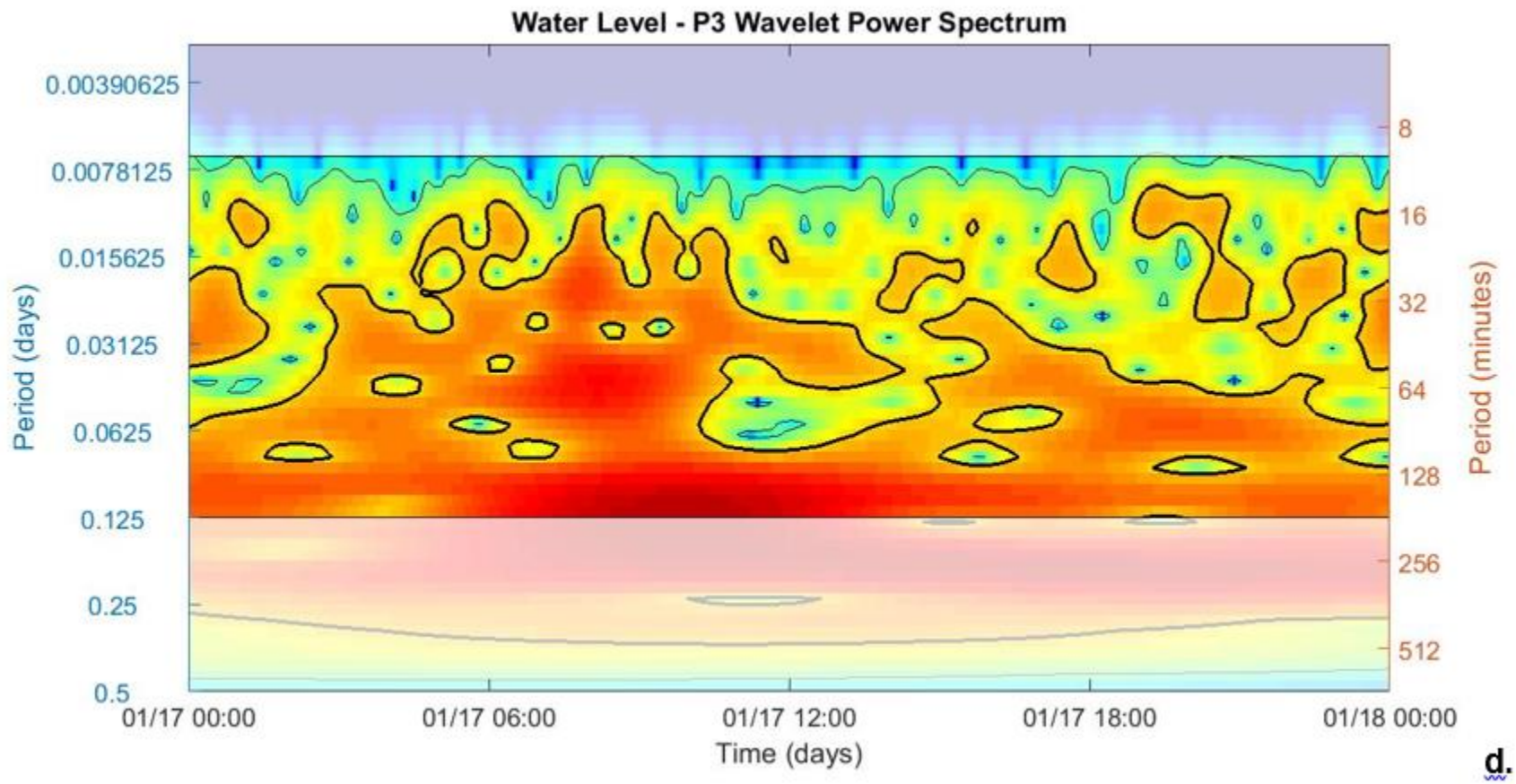


Figure 3-12: Continued

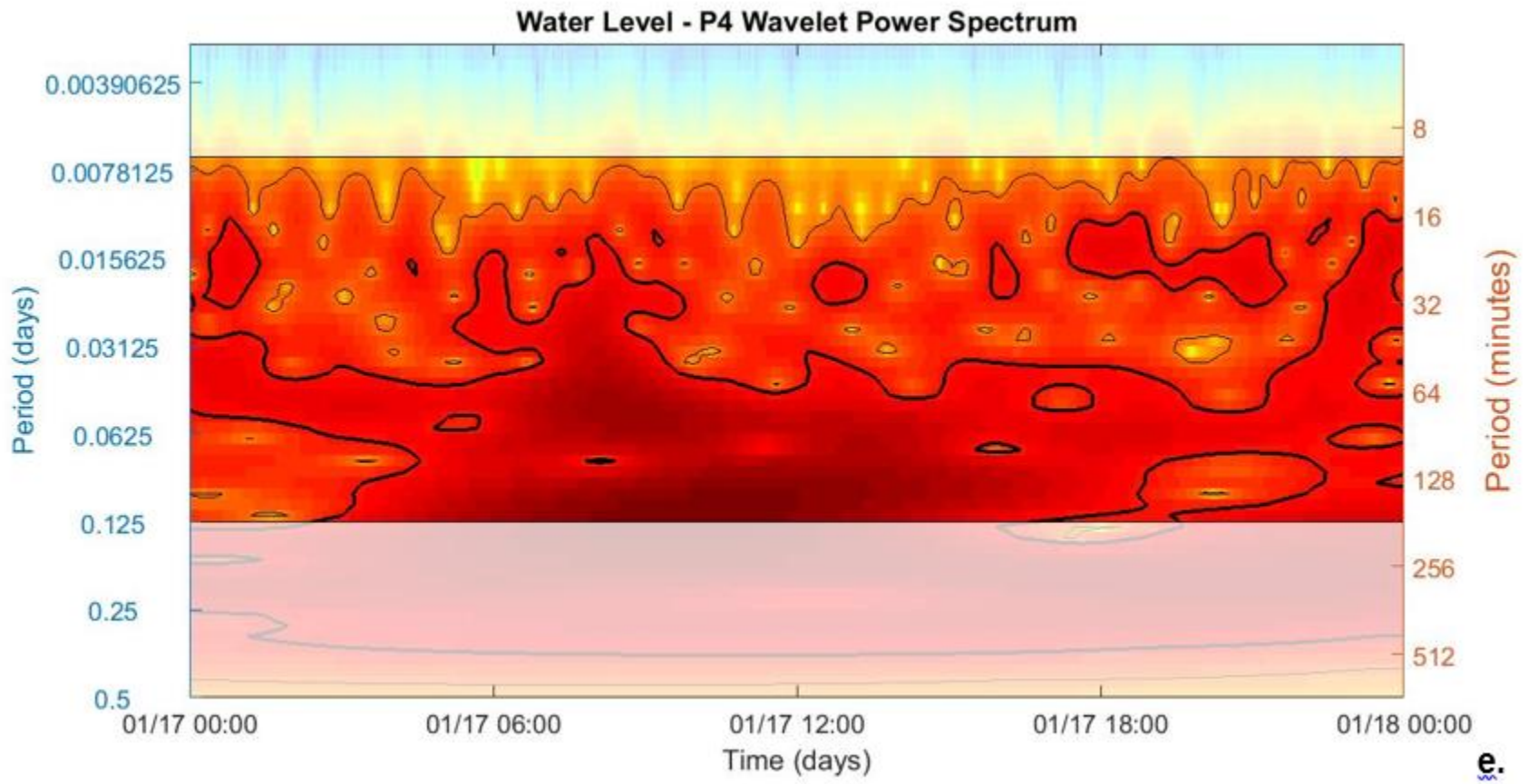


Figure 3-12: Continued

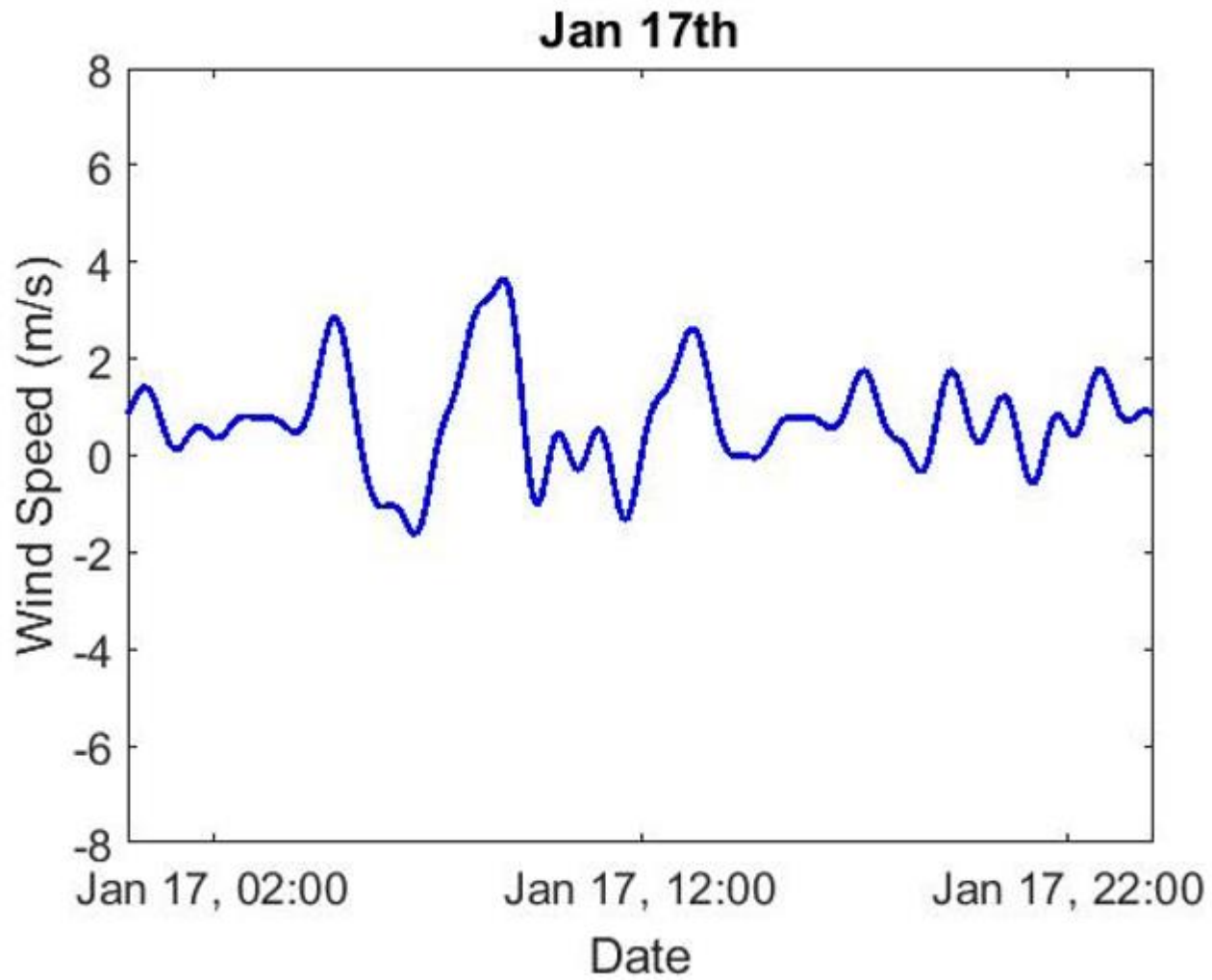


Figure 3-13: Filtered East-West wind record at PCB on January 17th, 2017.

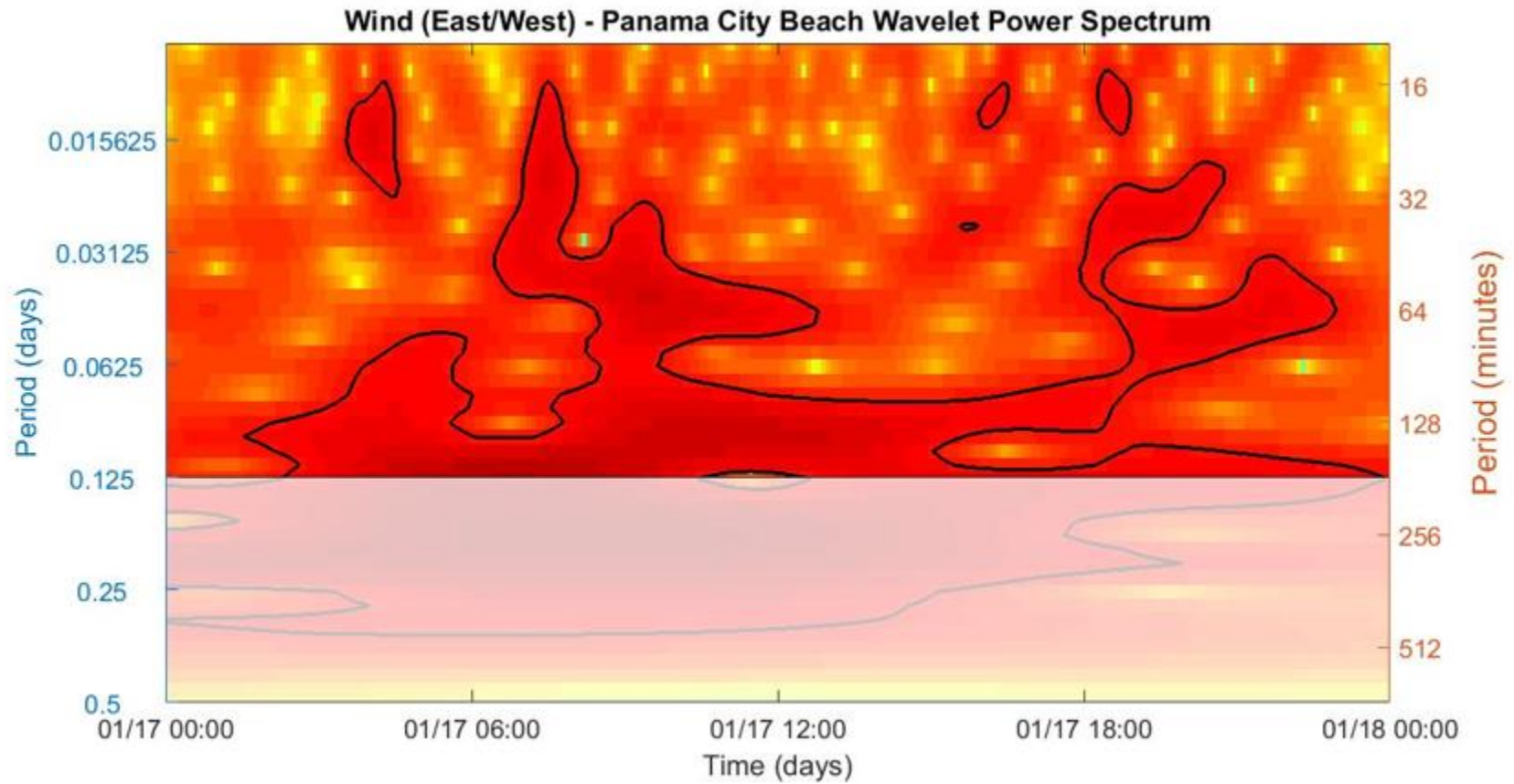


Figure 3-14: Wavelet analysis of wind signal on January 17, 2016 from PCB. Periods greater than 3 hours have been grayed out to indicate that they are outside of the meteotsunami frequency band.

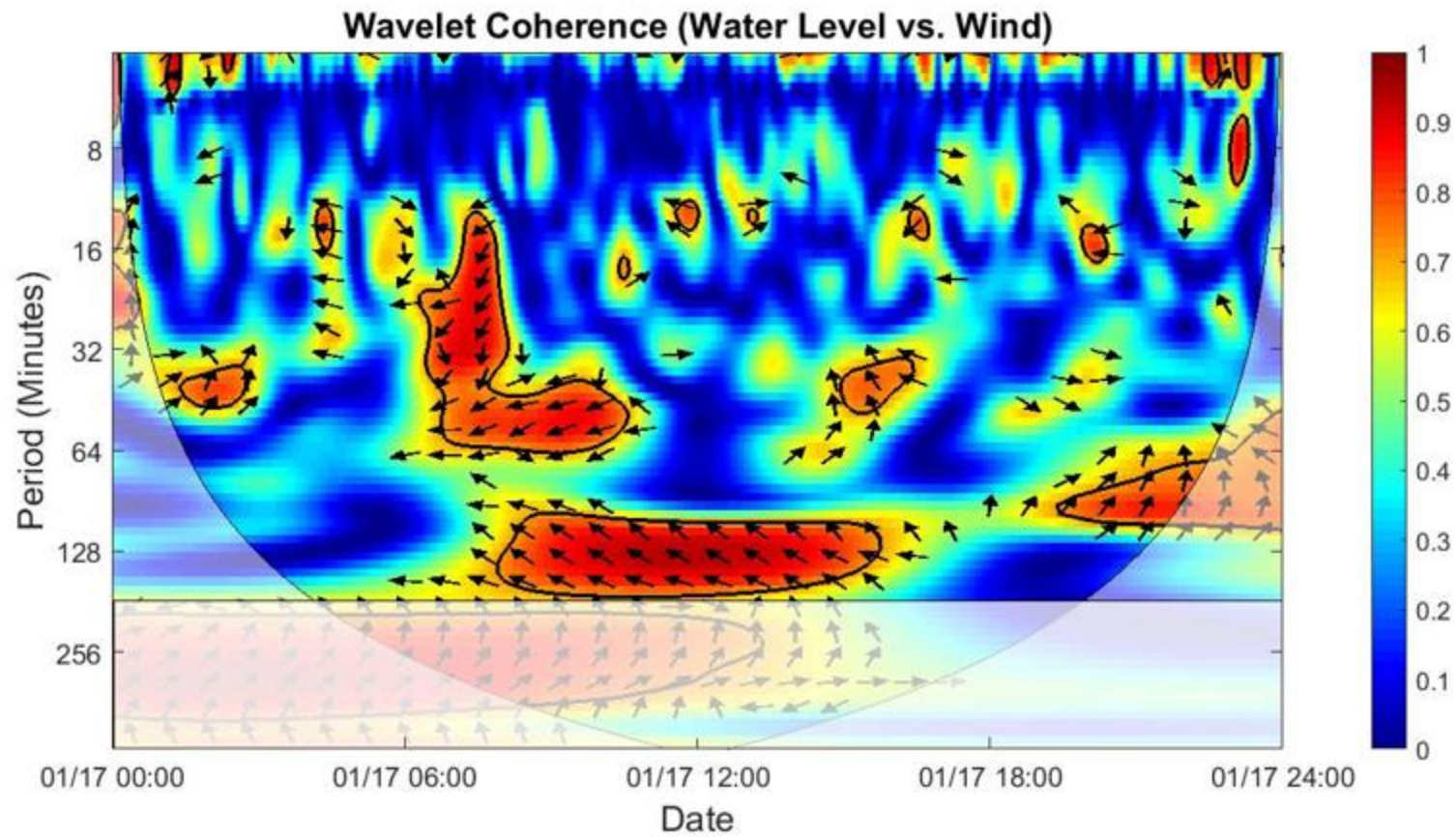


Figure 3-15: Wavelet coherence analysis of wind signal on January 17, 2016 from PCB. Arrows indicate the phase difference between the two signals. (Arrow pointing up indicates water level leads wind by 90°.

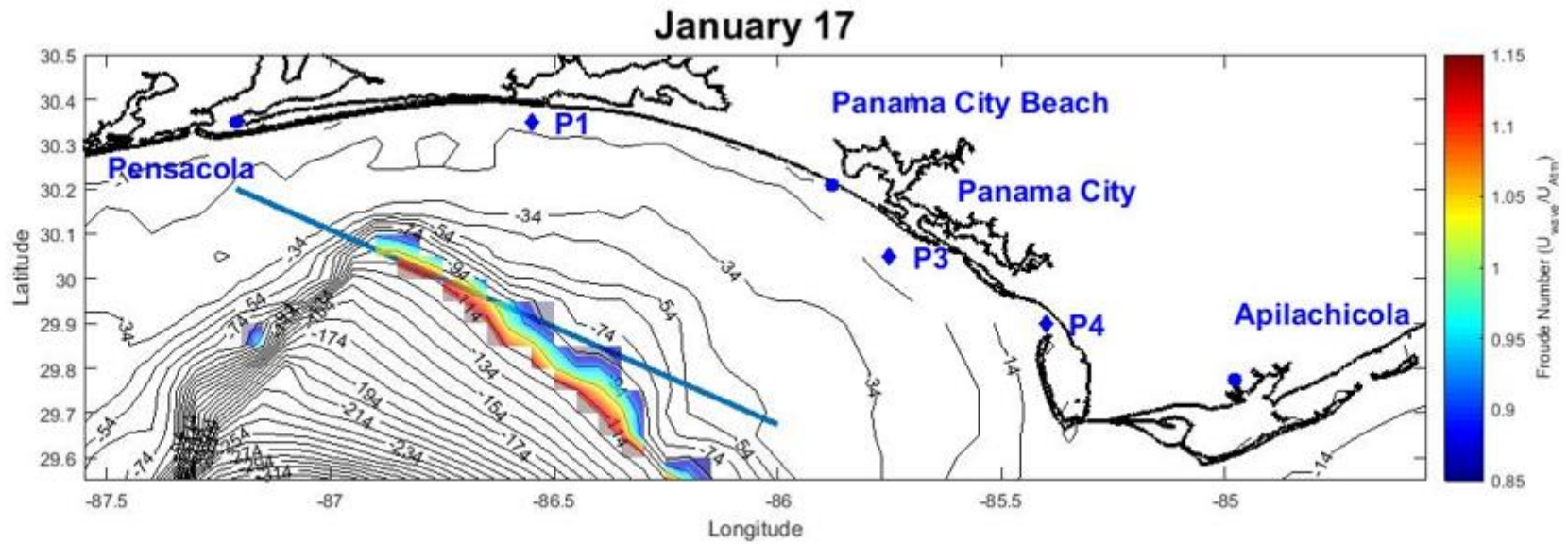


Figure 3-16: Spatial representation of the Froude number for the atmospheric system on January 17, 2016. The blue line indicates the propagation of the atmospheric disturbance, optimized for the maximum potential resonance.

CHAPTER 4 DISCUSSION

Possible meteotsunami generation mechanisms relate to instantaneous pressure jumps or trains of atmospheric gravity waves [Hibiya and Kajiuura, 1982; Vilibic' et al., 2004, 2005; Gossard and Munk, 1954; Monserrat et al., 1991a; Garcies et al., 1996]. In the Gulf of Mexico, it appears that the oscillatory motion seen in Figure 3-2 and Figure 3-10 is more indicative of wave trains causing meteotsunamis. The change in water surface elevation due to Proudman resonance can be given as [Proudman, 1929; Monserrat et al., 2006; Choi et al., 2008; Vilibic', 2008]:

$$\Delta\eta \propto \frac{\Delta\bar{\eta} \bar{C}^2}{\bar{C}^2 - U_a^2} = \frac{\Delta\bar{\eta}}{1 - Fr^2} \quad (4-1)$$

where $\Delta\bar{\eta} = \Delta P_a / (\rho g h)$ is the water level variation due to the inverse barometer effect, ΔP_a is the change in atmospheric pressure, g is the acceleration of gravity, and ρ is the density of water. The celerity $C = \sqrt{gh}$ is the shallow water wave celerity, where h is the water depth and U_a is the speed of the atmospheric disturbance. Rearranging, we can define the Froude number as $Fr = U_a / C$. As shown here, amplification increases as the Froude number approaches a value of 1. Additionally, as the Froude number approaches 1, the maximum elevation change is given by:

$$\Delta\eta = \frac{\Delta\bar{\eta}}{L} \frac{x_f}{2} \quad (4-2)$$

where $x_f = U_a t$ is the distance the pressure jump travels while resonance is present and L is the horizontal scale of the pressure jump.

Equation 4-2 was applied to both the January 15th and January 17th events to determine the maximum elevation change due to atmospheric pressure over the distances shown in Figure 3-9 and Figure 3-16. For both events, this approach yielded values that were one order of magnitude smaller than the water levels recorded by sensors. This discrepancy indicates that solely analyzing for atmospheric pressure is insufficient. Analytical expressions must be developed that include resonance caused by atmospheric pressure and wind oscillations.

For both of the meteotsunami events, wavelet analysis of water level and atmospheric pressure show similar frequency structures. Further analysis shows, however, that this similarity can be misleading. Wavelet coherence, which quantitatively measures the similarity of the signals, yielded little to no coherence between the two. January 15th wind records, when transformed into a wavelet spectrum, looked similar to the water level and atmospheric pressure signals, but only showed coherence with the water level signal. January 17th wind records do not visually resemble either the associated water level or atmospheric pressure signals, but still show coherence with the water level signal. While this does not prove that atmospheric pressure forcing is negligible, it does allow one to conclude that wind oscillations play a role in meteotsunami amplification. Again, further research is required to determine the balance, if any, that these two factors strike in the development of meteotsunamis.

The Gulf of Mexico, because of its extensive shelf bathymetry, provides a unique opportunity to study meteotsunami generation and propagation. Due to the influence of El Niño in winter 2015-2016, I was able to select from at least 9 atmospheric systems that had the potential to generate meteotsunamis. Such ability is rare in the study of meteotsunamis because of their unpredictability. A number of assumptions were made to determine the time at which the meteotsunamis on January 15th and January 17th became free waves. The first, and most crucial, is the existence of a well-structured convective system that travels as a plane (linear) wave. The atmospheric pressure and wind data presented here are from land-based sensors at least 40 km from the location where resonance should have occurred. If atmospheric data could be obtained from the geographical resonance area, it could be different from that obtained by a land-based sensor.

Other authors have used radar reflectivity values to determine the speed and direction of a 'front', assumed to be a term interchangeable with 'atmospheric pressure disturbance' [Sheremet et al., 2016; Vilibic et al., 2014]. The methods presented in this paper challenge this approach. As seen on January 15th, a clear squall line develops as the system propagates westward with a maximum rate of pressure change of 1.11 hPa/10mins. Such a squall line does not exist on January 17th, and yet the magnitude of the pressure change is about 50% higher. If the magnitude of the radar reflectivity value does not correspond to the magnitude of the pressure change, one should question whether the speed and direction of this squall line corresponds to the speed and

direction of the pressure disturbance. Still, a limitation of the results presented in this paper is the accuracy of the systems' calculated speed and direction using vector addition and assuming a plane wave. The 4 NOAA stations used in this study make a nearly straight line, limiting the effectiveness of triangulation. If another sensor existed (ideally in open water), more accurate speed and direction calculations would be possible.

A major limitation to this research is the absence of numerical modeling. A number of studies attempt to capture the behavior of meteotsunamis in numerical models [Vilibic et al., 2014; Whitmore and Knight, 2014], but the community has yet to provide an effective air-sea coupled model that can capture the effects of resonance. The information presented in this paper should be used in the future to identify the location where a meteotsunami becomes a free wave. Using numerical modeling, one could presumably create a meteotsunami wave at this location, free of resonant forcing, that would yield the same signal response on the coastline as the events of January 15th and January 17th. This approach would provide a specific amplitude of the wave at the point of separation and, comparing this to the wave size at the generation point (only influenced by the inverse barometer effect), one could quantify the amplification of a meteotsunami during this period of resonance.

In the future, at least 3 atmospheric pressure sensors should be deployed in the areas described by Figure 3-9 and Figure 3-16. Atmospheric pressure sensors will allow accurate characterizations of the geometry of an atmospheric pressure disturbance. Because meteotsunami studies use coastal sensors to

detect meteotsunamis, other types of forcing often muddle these signals (refraction, diffraction, shoaling, etc.). Sensors placed in open water will allow for a more focused study of meteotsunami amplification due to resonance.

As stated before, meteotsunamis can have devastating effects on coastal communities. These effects are especially intense when harbor resonance occurs. Because of this, further study should be considered to analyze the vulnerability of coastal inlets to meteotsunamis. Additionally, priority should be dedicated to developing a system that can accurately forecast meteotsunami events. The current limitation to this is a lack of spatial resolution for atmospheric pressure sensors. The results presented in this paper can serve as a basic characterization of conditions favorable for meteotsunami generation (speed, direction, and amplitude of pressure disturbance). Given better spatial resolution, these conditions could be monitored in real-time to suggest when coastal communities in the northeast Gulf of Mexico should expect meteotsunami activity.

CHAPTER 5 CONCLUSION

Metetsunamis are common in the northeastern Gulf of Mexico. The typical eastward propagation of atmospheric disturbances in the winter months makes Panama City and areas east of it particularly susceptible to these long wave phenomena. The results shown here demonstrate that metetsunamis of over 70 cm are possible and can be caused by atmospheric disturbances in multiple types of storm structures. Metetsunami appearance in the Gulf of Mexico is related to oscillatory motion in atmospheric properties. In addition to the atmospheric pressure signal, coherence between the metetsunami water level and oscillatory wind patterns indicates a relevant role of wind associated with convective systems. Lastly, this study presents a novel approach, using spatial Froude number representation, to identify the physical location of resonance and the point where an atmosphere-coupled wave becomes a free wave. Using this approach, future research can model a wave that starts at this location and propagates toward the shoreline, recreating a signal similar to established sensors. In this way, one can determine precisely how much amplification occurs during this resonance period, which in turn will allow for re-examination of current understanding of resonant mechanics.

LIST OF REFERENCES

- Asano T, Yamashiro T, Nishimura N (2012) Field Observations of Meteotsunami Locally Called “Abiki” in Urauchi Bay, Kami-Koshi Island, Japan. *Nat Hazards* 64:1685–1706
- Candela, J., Mazzola, S., Sammari, C., Limeburner, R., Lozano, C. J., Patti, B., and Bonnano, A. (1999) The “Mad Sea” Phenomenon in the Strait of Sicily. *J. Phys. Oceanogr.* 29:2210–2231
- Choi, B.-J., Y. Park, and K. Kwon (2008), Generation and Growth of Long Ocean Waves Along the West Coast of Korea in March 2007 [in Korean with English Abstract]. *Ocean Polar Res.* 30:453–466
- Churchill DD, Houston SH, Bond NA (1995) The Daytona Beach Wave of 3-4 July 1992: A Shallow-Water Gravity Wave Forced By a Propagating Squall Line. *Bull Am Meteorol. Soc.* 76:21–32
- Codiga, D.L. (2011) Unified Tidal Analysis and Prediction Using the UTide Matlab Functions,” Technical Report 2011-01, Graduate School of Oceanography, University of Rhode Island, Narragansett, RI. 59pp
- de Jong, M.P.C. and Battjes, J.A. (2004) Low-frequency Sea Waves Generated by Atmospheric Convection Cells. *Journal of Geophysical Research-Oceans* 109(C1), C01011
- Garcies, M., Gomis, D., and Monserrat, S. (1996) Pressure-forced Seiches of Large Amplitude in Inlets of the Balearic Islands. Part II: Observational Study. *J. Geophys. Res.* 101(C3):6453–6467
- Gossard, E. E. and Munk, W. H. (1954) On Gravity Waves in the Atmosphere. *J. Meteorol.* 11:259–269
- Greenspan, H. P. (1956) The Generation of Edge Waves by Moving Pressure Disturbances. *J. Fluid Mech.* 1:574–592
- Hibiya T. and Kajiwara K. (1982) Origin of the Abiki Phenomenon (a Kind of Seiches) in Nagasaki Bay. *J. Oceanogr. Soc. Japan* 38:172–182
- Monserrat, S., Ibberson, A., and Thorpe, A. J. (1991a) Atmospheric Gravity Waves and the “Rissaga” Phenomenon. *Quart. J. Roy. Meteorol. Soc.* 117:553–570
- Monserrat S., and Thorpe A.J. (1992) Gravity-wave Observation Using an Array of Microbarographs in the Balearic Islands. *Quart. J. Roy. Meteorol. Soc.* 118:259–282

- Montserrat S., Vilibić I., and Rabinovich A.B. (2006) Meteotsunamis: Atmospherically Induced Destructive Ocean Waves in the Tsunami Frequency Band. *Nat Hazards Earth Syst. Sci.* 6:1035–1051
- Morlet J., Arens G., Fourgeau E., and Giard D. (1982) Wave Propagation and Sampling Theory—Part II: Sampling Theory and Complex Waves. *Geophysics* 47(2):222-236
- Olabarrieta M., Valle-Levinson A., Martinez C.J. et al. (2017) Meteotsunamis in the Northeastern Gulf of Mexico and Their Possible Link to El Niño Southern Oscillation. *Nat. Hazards* 88: 1325-1346
- Orlić M. (1980) About a Possible Occurrence of the Proudman Resonance in the Adriatic. *Thalassia Jugosl.* 16(1):79–88
- Proudman J. (1929) The Effects on the Sea of Changes in Atmospheric Pressure. *Geophys. Suppl. Mon. Notices R. Astr. Soc.* 2(4):197–209
- Rabinovich A.B. and Monserrat S. (1996) Meteorological Tsunamis Near the Balearic and Kuril Islands: Descriptive and Statistical Analysis. *Nat. Hazards* 13(1):55–90
- Sallenger A.H. Jr, List J.H., Gelfenbaum G., Stumpf R.P., and Hansen M. (1995) Large Wave at Daytona Beach, Florida, Explained as a Squall-line Surge. *J. Coastal Res.* 11:1383–1388
- Sepic J. and Rabinovich A. B. (2014) Meteotsunami in the Great Lakes and on the Atlantic Coast of the United States Generated by the “Derecho” of June 29-30, 2012. *Natural Hazards* 74:75–107
- Sheremet A, Gravois U, and Shrira V. (2016) Observations of Meteotsunami on the Louisiana Shelf: A Lone Soliton with a Soliton Pack. *Nat. Hazards* 84:471–492
- Vilibić I. (2005) Numerical Study of the Middle Adriatic Coastal Waters Sensitivity to the Various Air Pressure Travelling Disturbances. *Ann. Geophys.* 23:3569–3578
- Vilibić I, Domijan N, Orlić M, Leder N, and Pasarić M (2004) Resonant Coupling of a Traveling Air-Pressure Disturbance with the East Adriatic Coastal Waters. *J. Geophys. Res.* 109:C10001. doi:10.1029/2004JC002279
- Vilibić I., Monserrat S., and Rabinovich A. B. (2014). Meteorological Tsunamis on the US East Coast and in Other Regions of the World Ocean. *Nat. Hazards* 74:1–9

Vilibić I., Monserrat S., Rabinovich A. B., and Mihanović H. (2008). Numerical Modelling of the Destructive Meteotsunami of 15 June 2006 on the Coast of the Balearic Islands. *Pure Appl. Geophys.* 165:2169–2195

Whitmore P. and Knight B. (2014) Meteotsunami Forecasting: Sensitivities Demonstrated by the 2008 Boothbay, Maine, Event. *Nat. Hazards* 74:11–23

BIOGRAPHICAL SKETCH

Matlack E. Gillin received a Bachelor of Science in Ocean Engineering from the United States Naval Academy in May 2010. He was then commissioned in the United States Navy as a Nuclear Submarine Officer. He attended Navy Nuclear Propulsion Training Command in Charleston, SC and Naval Propulsion Training Unit in Ballston Spa, NY before checking on-board USS MARYLAND in King's Bay, GA. He served on MARYLAND from 2012 to 2015, when he transitioned to Commander, Submarine Forces Atlantic in Norfolk, VA as a Submarine Watch Officer. He separated from active duty in July 2016 to pursue graduate studies at the University of Florida. He received a Master of Engineering in coastal and oceanographic engineering in December 2017.